



# CHORUS

This is the accepted manuscript made available via CHORUS. The article has been published as:

## Numerical investigation of multistability in the unstable flow of a polymer solution through porous media

Manish Kumar, Soroush Aramideh, Christopher A. Browne, Sujit S. Datta, and Arezoo M. Ardekani

Phys. Rev. Fluids **6**, 033304 — Published 25 March 2021

DOI: [10.1103/PhysRevFluids.6.033304](https://doi.org/10.1103/PhysRevFluids.6.033304)

# Numerical investigation of multistability in the unstable flow of a polymer solution through porous media

Manish Kumar,<sup>1</sup> Soroush Aramideh,<sup>1</sup> Christopher A. Browne,<sup>2</sup> Sujit S. Datta,<sup>2</sup> and Arezoo M. Ardekani<sup>1</sup>

<sup>1</sup>*Department of Mechanical Engineering, Purdue University,  
585 Purdue Mall, West Lafayette, Indiana 47907 USA*

<sup>2</sup>*Chemical and Biological Engineering, Princeton University, Princeton, NJ 08544*

The flow of viscoelastic polymeric fluids through porous media is common in industrial applications such as oil recovery and ground water remediation. Polymeric stresses can lead to an elastic induced instability of the flow. Here, we numerically study the flow of a polymeric fluid in a channel consisting of multiple diverging and converging physical constraints, mimicking the pore bodies and throats of an ordered porous medium. Inertial stresses here are negligible, and instead the flow is dominated by elasticity and viscosity; their relative effects are characterized by the Weissenberg number. There is a critical Weissenberg number below which eddies appear on the top and the bottom of each pore. Above the critical Weissenberg number, eddies form in different regions of the pores and multiple distinct unstable flow structures occur. The stretched polymeric chains inside the pore facilitate eddy formation, whereas relaxed chains lead to eddy free regions. We quantify the eddy area and correlations between the flow patterns of different pairs of pores, as well as polymeric stress and pressure drop across the tortuous channel to better understand the mechanism behind the observed flow patterns.

## I. INTRODUCTION

Polymers can impart elastic properties to fluids, producing non-Newtonian spatiotemporal flow features [1–5]. Understanding polymer flow in porous media is of particular importance for enhanced oil recovery (EOR)[6] and groundwater remediation [7, 8], where polymer additives have improved the displacement of trapped nonaqueous liquids for collection downstream [9–14]. The flow of viscoelastic mucus through arrays of pillars (2D porous media) is also important for the transport of gametes and embryos in the reproductive track [15] and the trapping of inhaled dust particles in the airways of lungs [16]. In confined geometries, the surrounding porous matrix strongly affects the spatial and temporal features of the flow [17–21]. For example, the presence of polymers can induce strong velocity fluctuations, locally increasing viscous forces, and subsequently promoting the displacement of trapped liquids [22–26]. Understanding the spatiotemporal details of these flow fluctuations is important for effective EOR and groundwater remediation, but also for other emerging applications such as controlling mixing and flow in lab-on-a-chip devices, filtration [27], and extrusion of polymeric resins during 3-D printing [28, 29]. However, the onset of flow instabilities and the resulting flow features are highly sensitive to polymer properties, flow geometry, and imposed flow conditions [30–32]. This sensitivity challenges experimental observations, leaving many open questions on how to control the flow structure for fluid recovery [1, 23, 24, 33–39].

Between the solid grains of a porous matrix are large bodies of fluid-filled void space, connected to neighboring pore bodies by relatively small throats. These bodies and throats are often modeled with a series of expansions and constrictions [17, 40–42]. Upstream of constrictions, persistent recirculating eddies often form [43–48] to minimize the extensional stresses associated with polymer chain alignment [49–53]. Polymers are elongated by these curved streamlines, relaxing on a characteristic timescale  $\lambda$ . For sufficiently high shear rates  $\dot{\gamma}$ , polymers are advected faster than they relax, producing strong flow fluctuations at high Weissenberg numbers  $Wi \equiv \lambda\dot{\gamma}$  [54–58]. This fluctuating flow is sometimes called “elastic turbulence” because its features are often reminiscent of traditional inertial turbulence [55–57], despite the absence of inertia, characterized by arbitrarily small Reynolds numbers  $Re \ll 1$ .

Microfluidic experiments have revealed a variety of complex spatiotemporal flow features produced by these instabilities [45, 46, 59–75]. However, in 3-D porous media—like those encountered in EOR and groundwater remediation—the role of higher connectivity, elevated disorder, and successive pores are expected to significantly alter the flow [21, 33, 34, 76–82]. In particular, the accumulation of stresses as polymers traverse successive pores can produce spatial variation in the dominant flow features [43, 44, 63, 64, 83, 84]. In the interesting case of dense pores, polymers are advected faster than they relax, kinetically trapping polymers within each pore. Surprisingly, this trapping can produce a bistability in the flow, where each pore switches stochastically between two distinct flow structures: an eddy-dominated structure, and an eddy-free structure [47]. The emergence of multiple persistent flow structures is consistent with some theoretical predictions [45, 85, 86], and is hypothesized to occur when polymers within a pore are locally kinetically trapped in an extended or coiled conformation respectively, and hence when polymers’ advection time scale is smaller than relaxation time scale. However, the details of how these structures arise are unclear, and the role of spatial and temporal correlations between pore-scale flow structures are still largely unknown. Despite advances

in imaging single-polymer conformations [2, 64, 87–94], microscopic flow details remain hard to access experimentally in highly unstable flow.

Here, we uncover the underlying physical mechanisms of this multistability using numerical simulations. We are able to directly probe the local stress fields, elucidating the physical mechanisms underlying flow structures. We further observe a new, relatively rare flow structure, where eddies transiently appear in the center of pores, prompting new experimental investigations. Finally, we probe spatial correlations on shorter time scales and longer length scales than possible experimentally, showing that weak positive correlations in flow structures can persist for many pores. These results help elucidate how the local accumulation of extensional stresses contribute to the formation of various persistent flow structures in unstable polymer solution flow. Understanding and controlling these multistable flow structures may aid the application of these flows to EOR, groundwater remediation, lab-on-a-chip devices, filtration, and 3-D printing technologies.

## II. PROBLEM SETUP

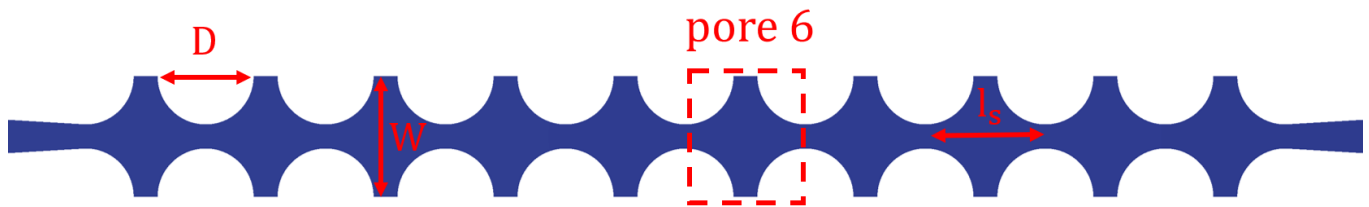


FIG. 1: The geometry used for numerical simulations.  $D = 1.6$  mm is the diameter of the pillar and  $W = 2$  mm is the width of the channel. The region enclosed with the square box depicts a sample pore.

In this work, we investigate the flow of viscoelastic fluid through a pore constriction array by performing two dimensional numerical simulations. The geometry used in the simulation to investigate the elastically-induced instability is a channel of width  $W$  with wall-centered pillar obstructions with diameter  $D$  (Fig. 1). The center-to-center separation of these pillars in the  $x$ -direction is varied from  $l_s = W$  for 10 closely spaced pores (Fig. 1) to  $l_s = 8W$  for two widely spaced pore throats (Fig. 5a). We also study the flow behavior in a single pore throat channel made of a single pair of wall-centered pillars (Fig. 2a). The Reynolds number ( $Re$ ) and Weissenberg number ( $Wi$ ) are the relevant dimensionless numbers.  $Re$  represents the ratio of inertial to viscous stresses and is given as  $Re = \rho U_t L_t / \eta$ , where  $\eta$  is zero-shear rate viscosity,  $\rho$  is fluid density,  $U_t$  is the average fluid velocity through the throat of the pore and length scale  $L_t$  is the half-width of the pore throat [95].  $Wi$  represents the ratio of elastic to viscous stresses and has been defined as  $Wi = N_1 / 2\tau_w$ , where  $N_1$  is the first normal stress difference and  $\tau_w$  is the shear stress. To estimate  $Wi$ , we use a planar rectilinear flow of a shear-thinning fluid obeying the FENE-P constitutive model through a slit of width same as the width of pore throat [95] and calculate  $Wi$  corresponding to the shear stress at the wall of the channel [96]. We use the time required to inject a single pore throat volume fluid as the characteristic time scale,  $t_{pv} = V_{pv} / Q$ , where  $V_{pv} = DW - \pi D^2 / 4$  is the pore throat volume per unit depth and  $Q$  is the volumetric flow rate per unit depth of the channel.

## III. GOVERNING EQUATIONS

The transient flow behavior of the incompressible fluid is governed by the conservation of mass and momentum:

$$\nabla \cdot \mathbf{u} = 0, \quad (1)$$

$$\rho \left( \frac{\partial \mathbf{u}}{\partial t} + \mathbf{u} \cdot \nabla \mathbf{u} \right) = -\nabla p + \nabla \cdot \boldsymbol{\tau}, \quad (2)$$

where  $\mathbf{u}$ ,  $p$  and  $\boldsymbol{\tau}$  are the flow field, pressure field and total stress tensor, respectively. The stress tensor  $\boldsymbol{\tau}$  consists of solvent stress  $\boldsymbol{\tau}_s$  and polymeric stress  $\boldsymbol{\tau}_p$ ,  $\boldsymbol{\tau} = \boldsymbol{\tau}_s + \boldsymbol{\tau}_p$ . The solvent stress tensor,  $\boldsymbol{\tau}_s$ , can be obtained as  $\boldsymbol{\tau}_s = \eta_s(\nabla\mathbf{u} + \nabla\mathbf{u}^T)$ , where  $\eta_s$  is the solvent viscosity. We use the FENE-P constitutive equation to calculate the polymeric stresses [76, 97]:

$$\boldsymbol{\tau}_p + \frac{\lambda}{f} \overset{\nabla}{\boldsymbol{\tau}}_p = \frac{a\eta_p}{f} (\nabla\mathbf{u} + \nabla\mathbf{u}^T) - \frac{D}{Dt} \left( \frac{1}{f} \right) [\lambda\boldsymbol{\tau}_p + a\eta_p\mathbf{I}], \quad (3)$$

where  $\lambda$  is the relaxation time of the polymer,  $\eta_p$  is the polymeric contribution to zero-shear rate viscosity  $\eta = \eta_s + \eta_p$ ,  $\mathbf{I}$  is identity tensor and  $\frac{D}{Dt}$  is the material derivative. Function  $f$  is given as:

$$f(\boldsymbol{\tau}_p) = \frac{L^2 + \frac{\lambda}{a\eta_p} \text{tr}(\boldsymbol{\tau}_p)}{L^2 - 3}, \quad (4)$$

where  $a = L^2/(L^2 - 3)$  and parameter  $L^2 = 3R_0^2/R_e^2$  measures the extensibility of the polymer chains [96, 97].  $R_0$  is the maximum allowable length of the polymeric chain and  $R_e$  characterizes the equilibrium length of the chain. A typical range of the parameter  $L^2$  found in the literature for FENE-P model is 10-1000 [76, 95, 97, 98] and FENE-P model reduces into an Oldroyd-B constitutive model in the limit of  $L^2 \rightarrow \infty$ . Operator  $\nabla$  used in equation 3 represents the upper convective time derivative and is given by:

$$\overset{\nabla}{\boldsymbol{\tau}}_p = \frac{D\boldsymbol{\tau}_p}{Dt} - \boldsymbol{\tau}_p \cdot \nabla\mathbf{u} - \nabla\mathbf{u}^T \cdot \boldsymbol{\tau}_p. \quad (5)$$

The numerical simulations are performed using a finite volume model using an open-source framework OpenFOAM [99] integrated with RheoTool [100]. The equations are discretized using the finite volume method and the log-conformation approach has been used to calculate the polymeric stress tensor with higher accuracy and robustness. The relation between the polymeric stress tensor and conformation tensor is given as:

$$\boldsymbol{\tau}_p = \frac{\eta_p}{\lambda} (f e^{\boldsymbol{\Theta}} - a\mathbf{I}), \quad (6)$$

where  $\boldsymbol{\Theta}$  is the logarithm of conformation tensor. The details of the numerical methodologies and the code validations can be found here [100, 101]. In our simulations, we change the relaxation time ( $\lambda$ ) from 0.02s to 0.5s to change  $Wi$ , while keeping  $\rho = 1 \text{ kg/m}^3$ ,  $\eta_p = 0.99 \text{ Pa.s}$ ,  $\eta_s = 0.01 \text{ Pa.s}$ ,  $L^2 = 625$  and volumetric flow rate per unit depth of the channel  $Q = 16.8 \text{ mm}^2/\text{s}$  constant throughout the study. The width of the pore throat is  $2L_t = 0.4 \text{ mm}$  and the average fluid velocity through the pore throat ( $U_t$ ) is given as  $U_t = Q/2L_t = 42 \text{ mm/s}$ . These parametric values of fluid lead to  $Wi \approx 10 - 47$ . The Deborah number ( $De = \lambda U_t/l_s$ ) can also be defined for 2-throats and 10-pores channels.  $De$  ranges from 0.05 – 1.3 for 2-throats channels and 0.42 – 10.5 for 10-pores channels in the present study. The polymer chains do not have sufficient time to relax before reaching to the next pore in 10 closely placed pores as  $De > 1$  for cases with  $Wi > 18$  and hence the interactions among the pores are expected. The effect of inertia in our study is negligible as  $Re$  is very small,  $Re \sim 10^{-5}$ . The elasticity number,  $El = Wi/Re \sim 10^6$ , can be defined to characterise the relative importance of elasticity and inertia. In the present study, the elastic forces dominate over the inertia as  $El(\sim 10^6)$  is very large. Therefore, the effect of the change in elastic modulus of fluid due to the change in  $\lambda$  does not have any significant effect on the results. We use  $t_{pv}$  as the characteristic time scale in the present study.  $t_{pv} = 0.07\text{s}$  is constant due to the fixed flow rate. We performed simulations for dimensional time  $t_{\max}^* = 1.0 \text{ s}$ , which corresponds to  $t_{\max} = t_{\max}^*/t_{pv} \approx 14$  and varies from  $t_{\max}^*/\lambda = 50$  at  $Wi = 10$  to  $t_{\max}^*/\lambda = 2$  at  $Wi = 47$ .  $t^*$  is dimensional time and  $t = t^*/t_{pv}$  is dimensionless time. The flow converges to steady state for  $t > 0.2$  at  $Wi = 0.3$  (almost Newtonian fluid) and for fluctuating flows instability becomes fully developed for  $t > 1$  (see Appendix, VII A). We use time interval  $t = 2 - 14$  to calculate the statistics. Here, the maximum simulation time ( $t_{\max} \approx 14$ ) is sufficient for the convergence of the statistics. We use  $1/t_{pv}$  to scale the frequency and viscous stress  $\eta U_t/L_t$  to normalize polymeric stresses and pressure. In the next section, we study the flow field and elastic-induced instability in the above mentioned geometry (Fig. 1) for three different cases: a single pore throat (Sec. IV A), two widely separated pore throats (Sec. IV B) and ten closely spaced pores (Sec. IV C).

## IV. RESULTS AND DISCUSSION

### A. Single pore throat

To investigate the polymeric flow instability in the porous media, we start our study with a relatively simple geometry. Therefore, first we consider a channel with a single pore throat and study the dynamics of polymeric fluid

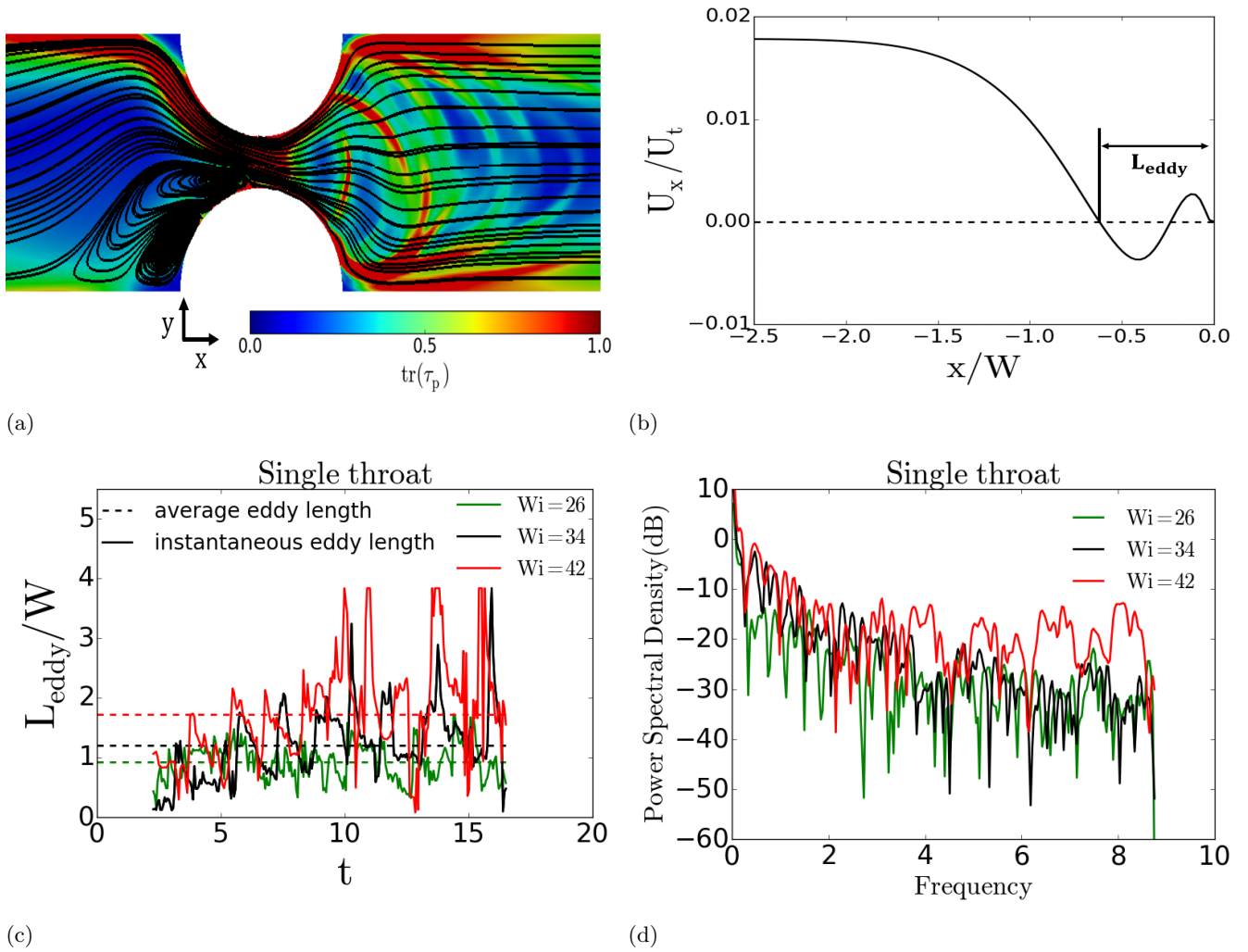


FIG. 2: (a) The streamlines depicting the eddies formation in the upstream of a single throated channel at  $Wi = 26$ . The contour represents the trace of polymeric stress tensor in the channel. (b) x-component of velocity along the length of channel close to the wall (at a distance  $\Delta y/W = 0.015$  from the wall, where  $\Delta y$  is the height of first grid element next to the wall). (c) The instantaneous and time-averaged length of eddies at different  $Wi$  in the upstream of a single pore channel. The time is non-dimensionalized with time scale  $t_{pv}$ . (d) Power spectral density (PSD) of the normalized eddies' length ( $L_{\text{eddy}}/W$ ). Frequency is normalized with  $1/t_{pv}$ .

flow in the channel. Eddies appear upstream of the throat (supplementary video 1). At  $Wi < Wi_{cr}$  these eddies form in both top and bottom regions. However, above a threshold  $Wi$  strong spatial and temporal fluctuations in flow velocity occur, leading to fluctuations in the position of eddies. Fluctuations are largely suppressed downstream of the pore throat, and eddy formation is weak [46, 47]. We can link these flow features to underlying polymer conformations by computing the polymeric stress tensor (Fig. 2a). The trace of polymeric stress tensor ( $\text{tr}(\tau_p)$ ) physically represents the elongation of the polymeric chains in the solution, where the higher value of trace corresponds to the larger stretching of the chains. In the high stress regions polymer chains are highly stretched, obstructing the fluid flow crossing the high stress regions and facilitating the flow separation (i.e., formation of eddies). In the upstream, the streak of large  $\text{tr}(\tau_p)$  are detached from the wall and goes into the middle of the constriction, indicating high polymer elongation, which drives eddy formation upstream of the constriction. The low value of  $\text{tr}(\tau_p)$  within the upstream eddy indicates that eddy formation reduces polymer stress (Fig. 2a). Polymeric chains inside the channel in the downstream of the throat are relaxed as the high polymeric stress regions occur close to the walls (Fig. 2a), which facilitates the divergence of the flow inside the channel and makes downstream region eddy free. Downstream of the constriction there appear to be waves of higher polymer extension being advected further downstream. To quantify the length of eddies ( $L_{\text{eddy}}$ ) upstream of the throat, we plot x-component of velocity ( $U_x$ ) at a distance  $\Delta y/W = 0.015$  ( $\Delta y$  is the height of first

grid element next to the wall) away from the wall (Fig. 2b).  $L_{\text{eddy}}$  is the length measured from the first stagnation point (left most of the throat) to the start of the throat (i.e.  $x = 0$ ). Thus,  $L_{\text{eddy}}$  covers all the upstream eddies shown in Fig. 2a. If eddies appear on both top and bottom regions,  $L_{\text{eddy}} = \max(L_{\text{eddy}}^{\text{top}}, L_{\text{eddy}}^{\text{bottom}})$ . We have plotted  $L_{\text{eddy}}$  in the upstream of the pore throat at different  $Wi$  (Fig. 2c). The instantaneous length of eddies fluctuates with time. However, the time-averaged length of eddies along with the intensity of fluctuations increases as  $Wi$  increases (Fig. 2c). These findings are consistent with the experimental observations [43, 45, 47, 48, 50–53, 68, 83, 102–105].

The power spectral density (PSD) of the normalized instantaneous eddy length depicts the strength of variations of  $L_{\text{eddy}}$  at different frequencies (Fig. 2d). The dimensionless frequency spectrum of the fluctuation of  $L_{\text{eddy}}$  is in the range of 0-9 (Fig. 2d). The PSD of smaller frequencies is larger than that of higher frequencies. The PSD of larger frequencies increases with  $Wi$ , which shows the increase of temporal fluctuations of  $L_{\text{eddy}}$  with  $Wi$ . We also study the statistics of  $L_{\text{eddy}}$  at different  $Wi$  in a single throated channel (Fig. 3a and 3b). The probability distribution of eddies' length ( $L_{\text{eddy}}$ ) shows that the range of  $L_{\text{eddy}}$  increases with  $Wi$  (Fig. 3a). We have plotted the mean ( $\mu$ ) and standard deviation ( $\sigma$ ) of normalized eddies' length ( $L_{\text{eddy}}/W$ ) to further quantify the range of eddies' length (Fig. 3b). The standard deviation monotonically increases with  $Wi$ , however the slope of  $\sigma$  changes between  $Wi = 26 - 30$ . Therefore, we define  $Wi_{\text{cr}} = 28 \pm 2$  as the onset of instability in a single throated channel. Fig. 3b also shows that the mean ( $\mu$ ) of  $L_{\text{eddy}}$  increases with  $Wi$ .  $Wi_{\text{cr}}$  based on the change in the slope of  $\sigma$  is simply a choice made that does not influence any of the interpretations, and a different choice made by defining  $Wi_{\text{cr}}$  as the change in the slope of  $\mu$  gives similar  $Wi_{\text{cr}}$  values.

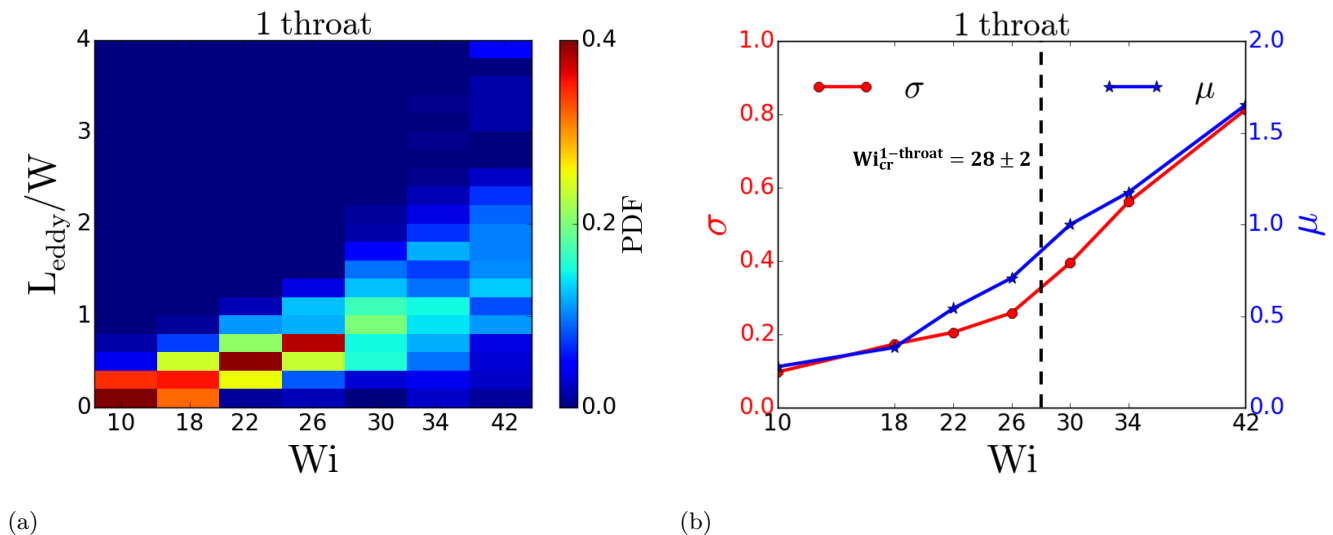


FIG. 3: (a) Probability density function of dimensionless eddy length ( $L_{\text{eddy}}/W$ ) in a single throated channel. (b) Mean ( $\mu$ ) and standard deviation ( $\sigma$ ) of normalized eddies' length.

## B. Two widely separated pore throats

After analyzing the flow dynamics in a channel with a single pore throat, we consider a channel with two widely separated pore throats ( $l_s = 8W$ ) (video 2). The eddies in front of each throat are unstable and the strength of fluctuations increases with  $Wi$  (Fig. 4). Similar to the single throat channel, the detachment of a streak of large  $\text{tr}(\tau_p)$  from the wall leads to eddy formation in the upstream of each throat, whereas high  $\text{tr}(\tau_p)$  close to the wall corresponds to eddy free region downstream of the throat (Fig. 5a). We also observe the waves of higher polymer extension being advected further downstream of each throat. We do not find any strong correlation between the length of eddies in the upstream of pore throats (Fig. 5b). However, we note that the time-averaged length of eddies upstream of first pore throat is slightly larger than that of the second pore throat (Fig. 4). To quantify instantaneous correlation between  $L_{\text{eddy}}$  of first and second throat, we define a correlation function  $f_{1,2}$  as:

$$f_{1,2} = 1 - \frac{2|(L_{\text{eddy}})_1 - (L_{\text{eddy}})_2|}{\max((L_{\text{eddy}})_1, (L_{\text{eddy}})_2)}, \quad (7)$$

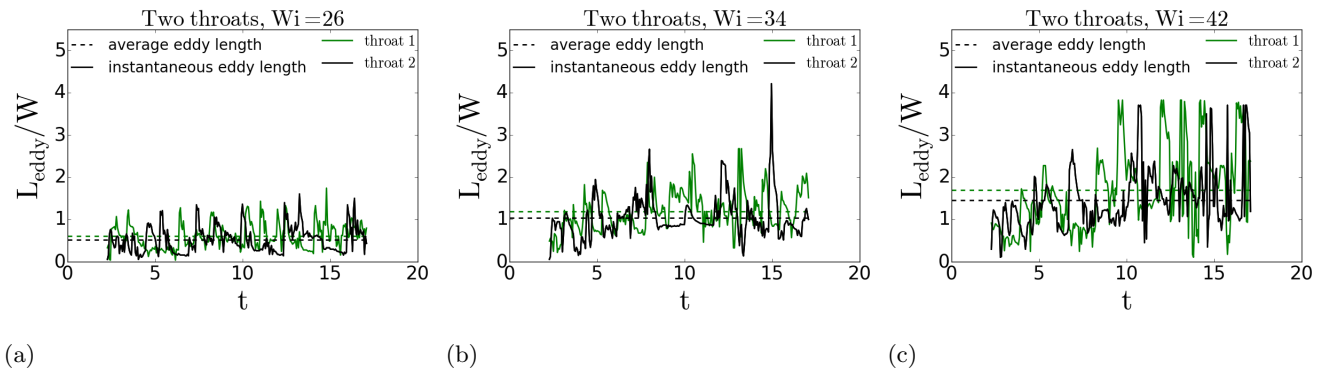


FIG. 4: The instantaneous and time-averaged length of eddies in the upstream of throat-1 and throat-2 at different  $Wi$  of a double throated channel. Time is normalized with volumetric flow time scale  $t_{pv}$ .

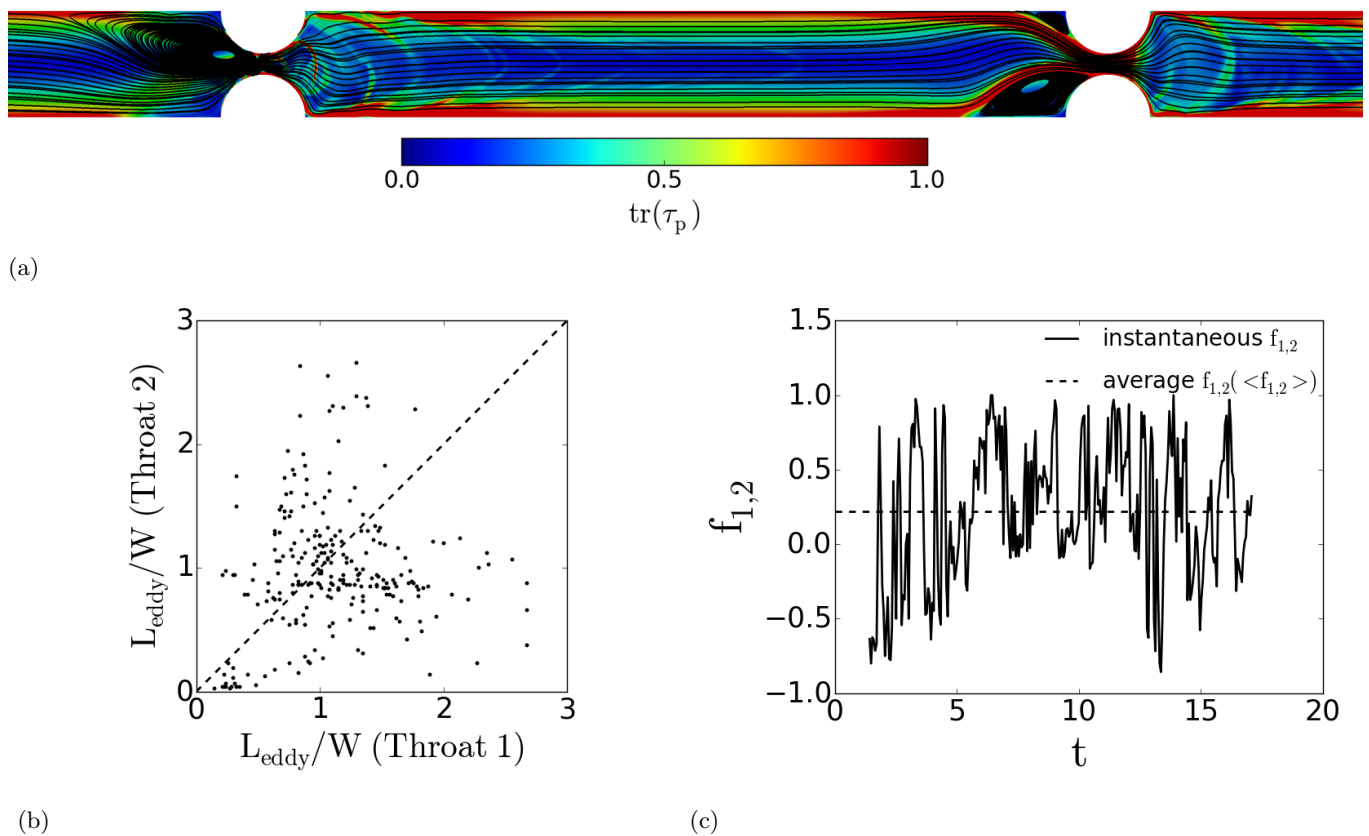


FIG. 5: (a) Streamlines and trace of polymeric stress tensor in a channel with two throats at  $Wi = 34$ . (b) The correlation between instantaneous eddy lengths of throat-1 and throat-2 at  $Wi = 34$  in a channel of two pore throats. (c) Instantaneous  $f_{1,2}$  and time-average  $\langle f_{1,2} \rangle$  value of the correlation function between the eddy of throat 1 and throat 2 at  $Wi = 34$ .

where  $f_{1,2} \rightarrow 1$  corresponds to similar eddies upstream of both throats, whereas  $f_{1,2} \rightarrow -1$  implies maximum difference between the length of eddies (Fig. 5c). The polymeric stress relaxation downstream of the first throat (except in the region very close to the wall, where the polymer is strongly stretched) can hinder the eddy formation upstream of the second throat (Fig. 5a). Due to large separation between the throats ( $De < 1$ ), the effect of the first throat on the eddy formation upstream of the second throat is small. This encourages the study of closely located throats ( $De > 1$ ), where high polymeric stress regions formed by one throat can easily interact with that of neighboring throat. As  $Wi$  is increased, the enhanced stretching of polymers leads to the formation of longer eddies. The difference between

the average length of eddies upstream of first and second throats also increases with  $Wi$  (Fig. 4), because the high polymeric stress region downstream of first throat has stronger impact on the eddies upstream of second throat as  $Wi$  increases.

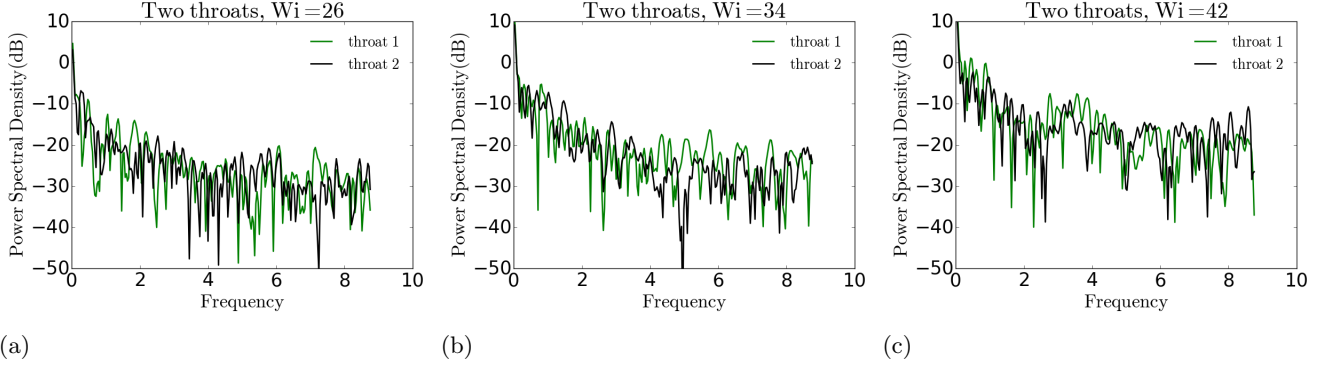


FIG. 6: Power spectral density of normalized eddies' length ( $L_{\text{eddy}}/W$ ) at (a)  $Wi = 26$ , (b)  $Wi = 34$  and (c)  $Wi = 42$ .

We have also plotted the power spectral density of the normalized eddy length in Fig. 5 to visualize the fluctuations frequency spectrum. Similar to the single throated channel, the PSD of  $L_{\text{eddy}}$  in the double-throated channel also increases with  $Wi$ , which corresponds to an increase in the fluctuations of  $L_{\text{eddy}}$  with  $Wi$ . Fig. 7a depicts the probability density function (PDF) of eddies' length in the channel of two widely separated throats. We quantify the standard deviation ( $\sigma$ ) and mean ( $\mu$ ) of  $L_{\text{eddy}}$  in Fig. 7b. Both,  $\sigma$  and  $\mu$  increase with  $Wi$ . We consider  $Wi_{\text{cr}} = 28 \pm 2$  as the threshold of the instability as the slope of  $\sigma$  changes between  $Wi = 26 - 30$ .

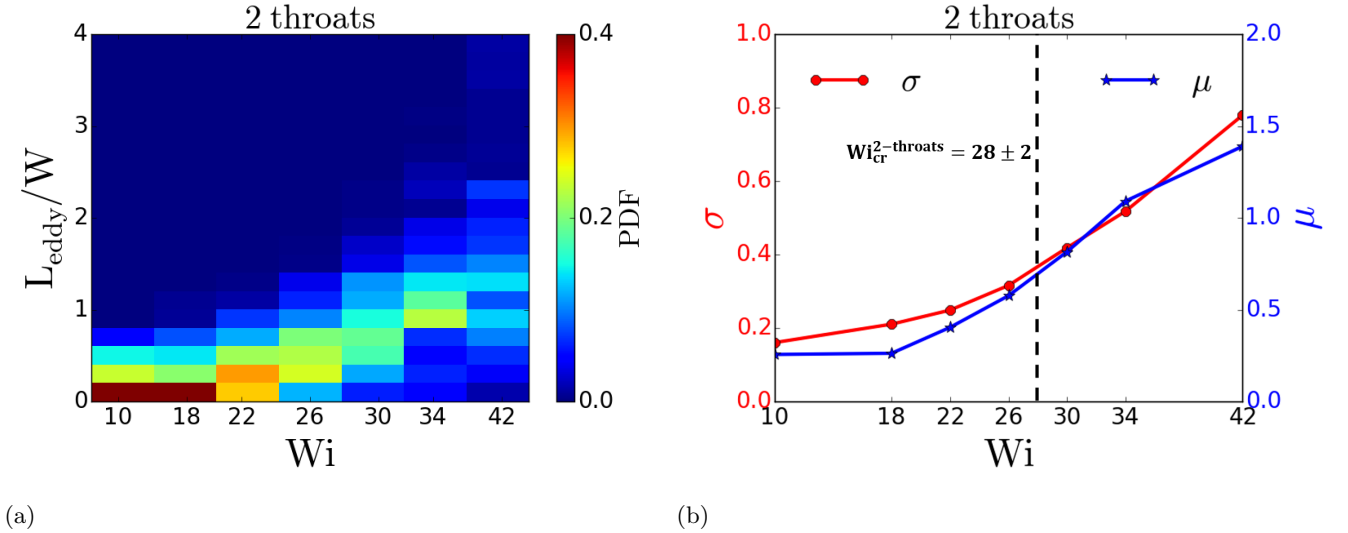
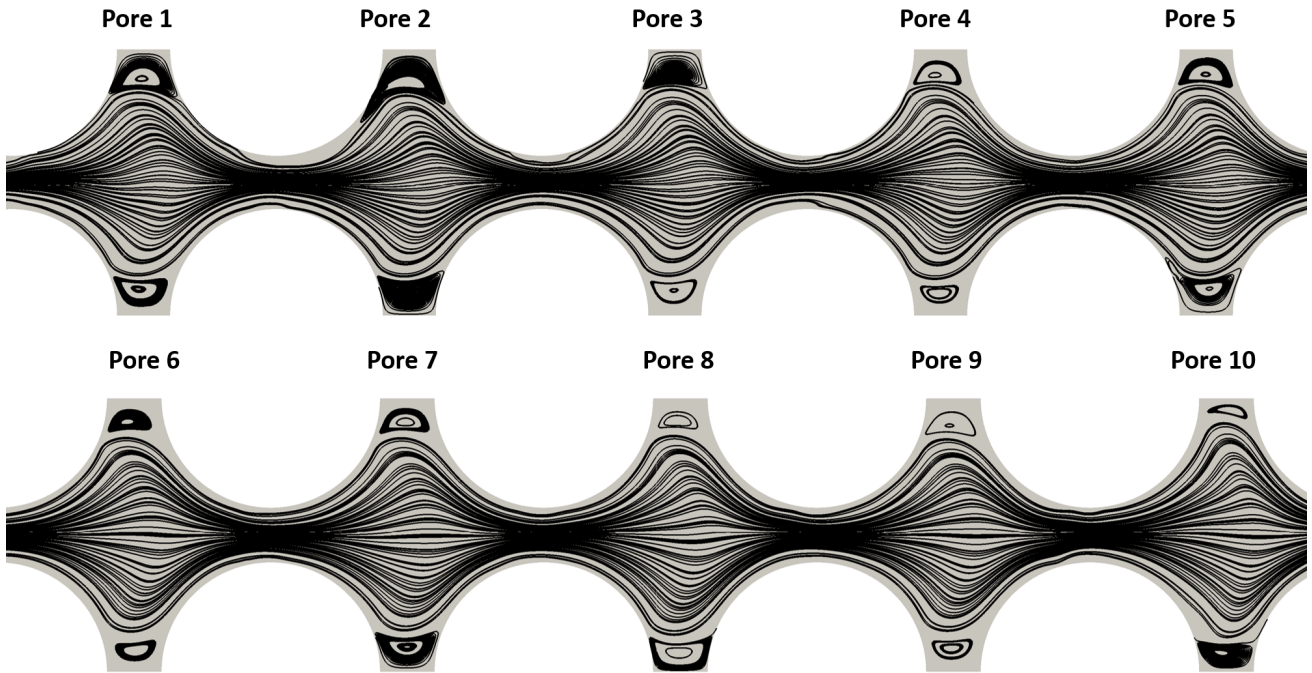


FIG. 7: (a) Probability density function of dimensionless eddy length in two widely separated throats channel. (b) Mean ( $\mu$ ) and standard deviation ( $\sigma$ ) of normalized eddies' length.

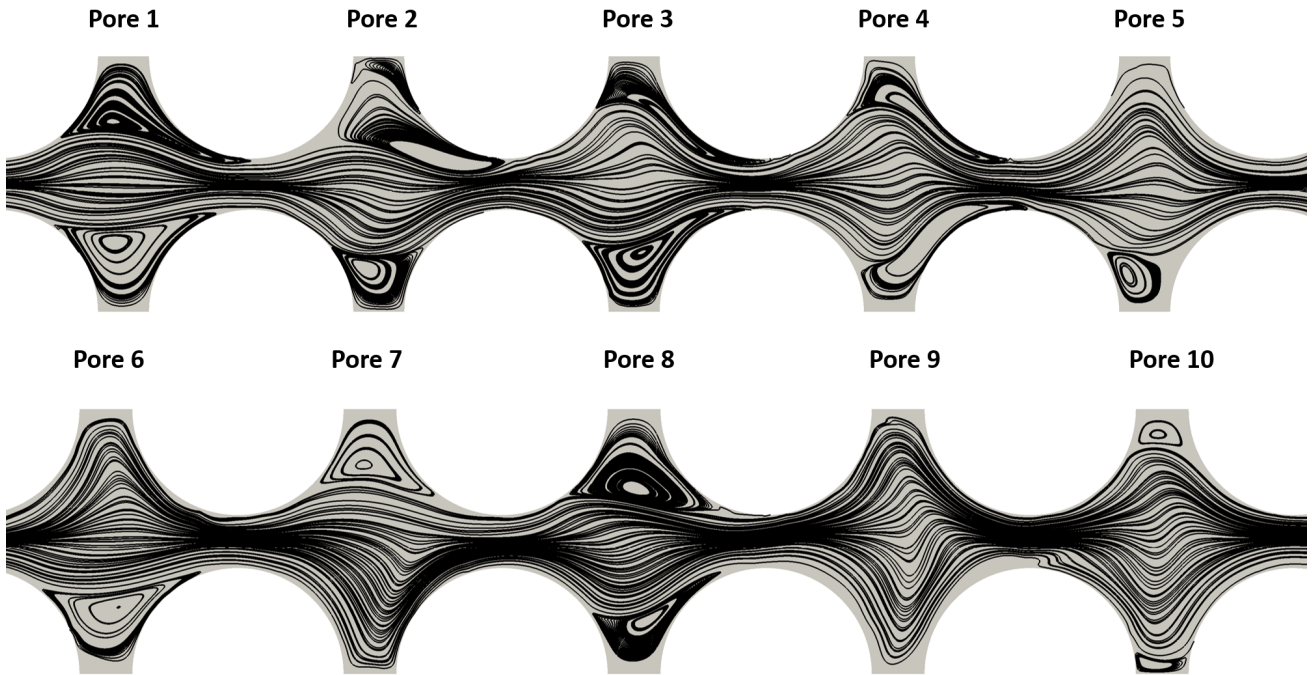
### C. Ten closely located pores

The study of single and double throated channels reveal the eddy formation on the upstream of the throat and the eddy free region downstream of the throat. These two contradictory behaviors compete in the region enclosed between closely located throats (i.e., pores) and determine the flow pattern inside the pore. Here, we study the dynamics of flow of the polymeric fluid inside 10 identical closely ( $l_s = W$ ) interconnected pores (Fig. 1). For a Newtonian fluid, stable eddies appear on the top and bottom of each pore (Appendix, VII B). At  $Wi < Wi_{\text{cr}}$ , the flow of polymeric fluid inside the pores forms eddies on the top and bottom of each pore (see supplementary video 3), whereas at  $Wi > Wi_{\text{cr}}$ ,





(a)



(b)

FIG. 8: (a) Instantaneous streamlines in a channel of 10 closely interconnected pores at  $Wi = 18$  and dimensionless time,  $t \approx 6$ . (b) Instantaneous streamlines in a channel of 10 closely interconnected pores at  $Wi = 34$  and dimensionless time,  $t \approx 10$ .

the eddy on the top as well as bottom of the pores collapse and reform (supplementary video 4). At  $Wi = 18 (< Wi_{cr})$ , all the pores in the channel have a similar eddy pattern (Fig. 8a). Fig. 8b depicts the snapshot of streamlines across

the pores at  $Wi = 34 (> Wi_{cr})$ . The pattern of polymeric fluid flow inside the pore at  $Wi = 34$  can be divided into 4 distinct types (Fig. 8b): (1) eddies on both top and bottom regions of pore (i.e., pore 8), (2) eddy free bottom region of pore (i.e., pore 7), (3) eddy free pore (i.e., pore 9) and (4) eddy free top region of pore (i.e., pore 6). These patterns are unstable and interchange frequently (video 4). Often the size of eddies at  $Wi > Wi_{cr}$ , when the eddies appear on both top and bottom of the pore (pore type-1), is different (i.e., pore 2). These coherent flow structures (i.e., multi-stability) (Fig. 8b), that are persistent in time despite the underlying unstable flow, have been also reported in experiments [47].

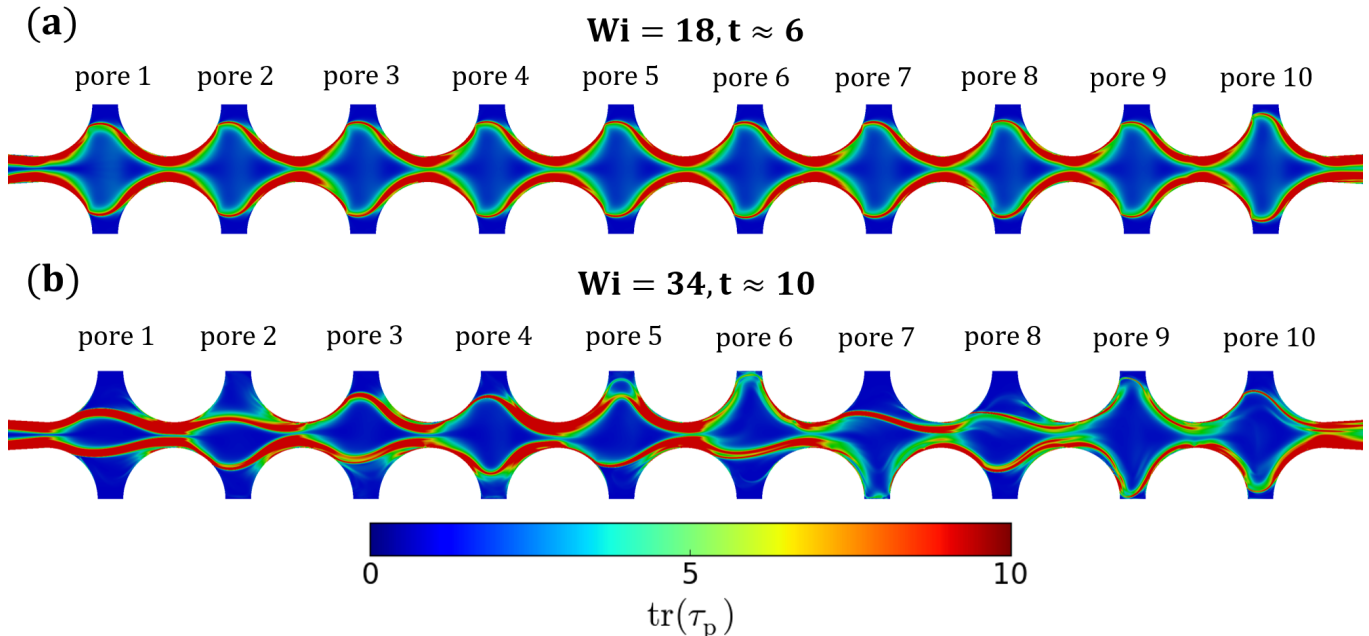


FIG. 9: The snapshot of the trace of polymeric stress tensor at (a)  $Wi = 18, t \approx 6$  and (b)  $Wi = 34, t \approx 10$ . These plots of trace of polymeric stress correspond to the streamlines shown in Fig. 8a and Fig. 8b, respectively.

The flow structure in each pore is closely coupled to the underlying polymeric stress field, which controls the local rheology. For the flow at  $Wi = 18 < Wi_{cr}$ , the two regions of high polymeric stress in the top and bottom of the pore correspond to the regions where the flow separated from the wall to form eddies (Fig. 8a and 9a). The polymer stress profile is similar among the pores at  $Wi < Wi_{cr}$  ( $Wi = 18$ ), therefore we see a similar flow pattern in different pores. At  $Wi > Wi_{cr}$ , both the polymeric stress field and the velocity field are unstable and vary between pores (Fig. 8b and 9b). The multi-stability of the flow pattern inside the pores at  $Wi = 34$  (Fig. 8b) can be explained with the help of corresponding high polymeric stress regions shown in Fig. 9b. There are two high stress regions in the middle of the eighth pore, which coincide with the formation of eddies on the top and the bottom of the pore. Everywhere inside the ninth pore, the polymeric chains are unstretched (i.e., the high stress regions only occur close to the walls), and hence the flow diverges in this pore and we do not see any eddy. High polymeric stress occurs in the top region of the seventh pore, therefore an eddy appears only in the top region of the pore and the bottom region is eddy free. Conversely, there is a high stress region in the bottom region of the sixth pore, and therefore the eddy forms only in the bottom region of the pore. Thus, the stretched polymeric chains inside the pore lead to eddy formation, while coiled chains lead to eddy free regions. This explanation also holds for the other pores in Fig. 8b. Similarly, a streak of high stress has been observed in the wake of a confined cylinder in a complex fluid [75, 84]. The asymmetric flows of polymeric fluids in cross-slot geometries also exhibit streaks of high stress [106–109].

Now, we study the time dependent behavior of an individual pore. We quantify the area occupied by eddies on the top and bottom regions of the second pore separately (Fig. 10a). At  $Wi < Wi_{cr}$ , we always observe eddies on both the top and bottom regions of the pore (Fig. 10a). Whereas, the size of both eddies is constant at  $Wi = 0.3$  (Appendix, VII B). To visualize the time dependent behavior of high polymeric stress regions, we plot the contours of trace of polymeric stress tensor across the channel at the center of the second pore (i.e., along the red line shown in the inset of Fig. 10a) in Fig. 10b. The peak value of the trace of polymer stress tensor corresponds to the flow-separation region (i.e., the distance from the wall of the channel, where streamlines separate from the main flow and form a closed streamline to make eddies). The contour of the trace of polymer stress also has two distinct regions well inside the pore where the maximum value of polymer stress tensor occurs, which further supports the presence of two distinct

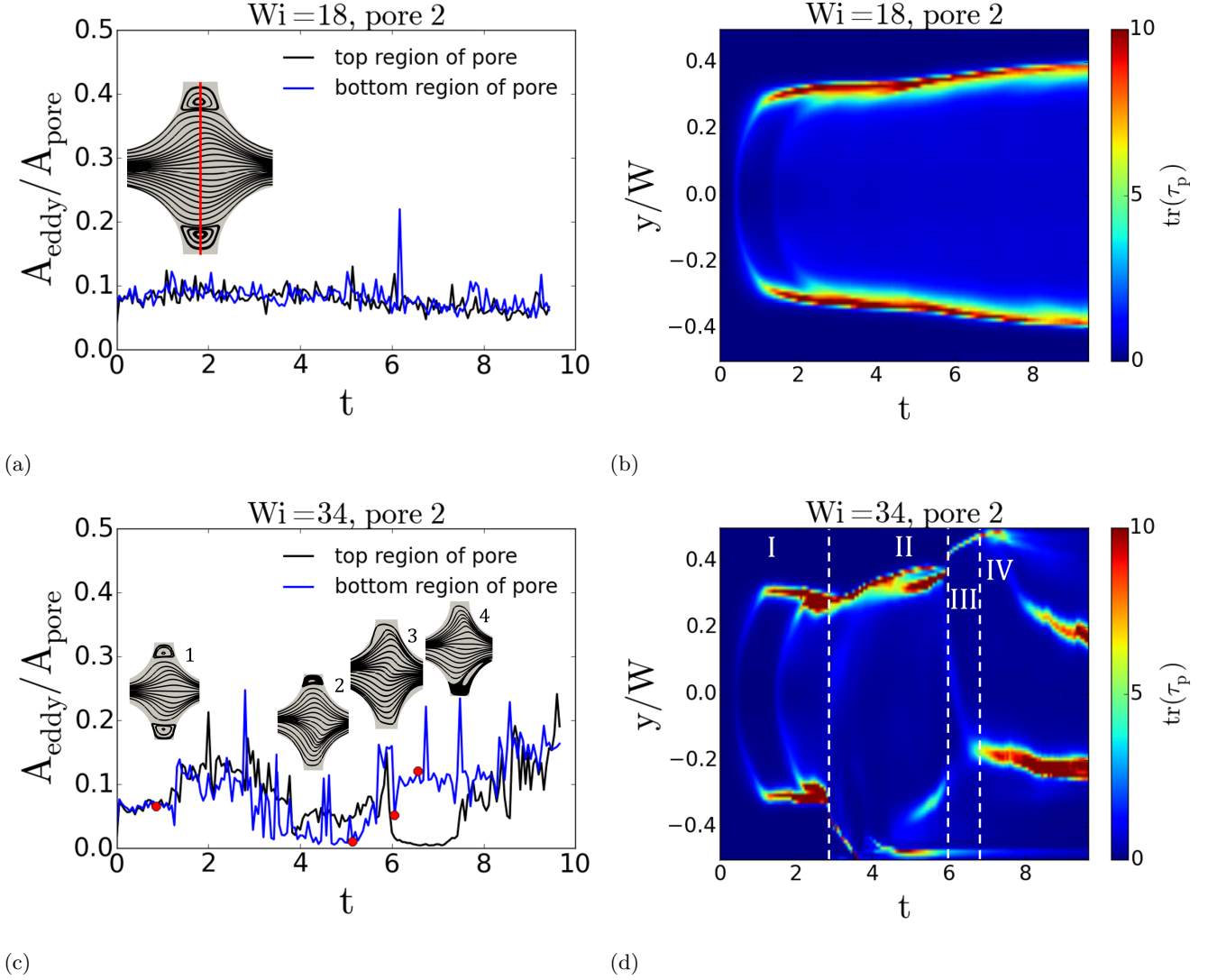


FIG. 10: (a) The ratio of eddy to pore area for “pore 2” as a function of time at  $Wi = 18$ .  $A_{\text{eddy}}$  is the area of eddies in a particular half region of the pore, while  $A_{\text{pore}}$  is the total area of the pore. The streamlines inside the pore represent the flow pattern at  $Wi = 18$ . (b) The contour of the trace of polymeric stress tensor across the channel at the center of the pore (i.e., along the red line shown in the inset of Fig. 10a). (c) The ratio of eddy to pore area for “pore 2” as a function of time at  $Wi = 34$ . The snapshots of streamlines inside the pore represent the flow pattern at specific time indicated by red solid circles. (d) The contour of the trace of the polymer stress tensor across the channel at the center of the pore. The upper limit of time in these plots ( $t = 9.5$ ) corresponds to  $t^*/\lambda = 13.4$  for  $Wi = 18$  and  $t^*/\lambda = 3.3$  for  $Wi = 34$ .

regions where flow separation takes place (Fig. 10b).

The flow pattern inside the pore is transient at  $Wi > Wi_{\text{cr}}$  and each pore can exhibit all 4 kinds of flow patterns discussed earlier. The area of eddies, whether it is in the top region or bottom region of the pore, fluctuates (Fig. 10c). The transition from one flow pattern to another can be easily seen in Fig. 10c. There are eddies on the top as well as bottom regions of the pore in the beginning of the simulation (flow pattern type-1), but the area of eddies is not identically equal and the difference between the area of eddies increases with time. Eventually, the eddy in the bottom of the pore completely disappears and a new flow state with an eddy only on the top region of the pore (type-2) emerges. Next, both eddies disappear and the pore becomes completely eddy free (type-3). Finally, the eddy in the bottom region of the pore again reappears and it leads to the formation of a different flow state inside the pore, where the top region of the pore is eddy free and bottom region has eddy (type-4). Thus, the flow patterns of the polymeric fluid inside the pore are transient. Other pores in the channel also exhibit similar transitions, though the

switching between flow states does not show any clear pattern. As  $Wi$  ( $> Wi_{cr}$ ) increases, the distinct flow structures change even more frequently.

The time dependent flow patterns inside the pore at  $Wi > Wi_{cr}$  (Fig. 10c) can be explained using the trace of polymeric stress tensor across the channel at the center of the pore (Fig. 10d). Part-I of Fig. 10d depicts that there are two distinct regions, approximately equidistant from the walls, where maximum values of the trace of polymer stress occur. This distribution of stress corresponds to a pattern where both top and bottom regions of the pore have eddies (pore type-1 in Fig. 10c). Part-II has a single region inside the pore with peak value of trace of polymer stress and it lies on the top region of the pore. The local peak value of trace of polymer stress in the bottom region of the pore lies close to the wall and is much smaller than the global maximum. This stress distribution represents the pattern where top region of the pore has an eddy and bottom region of the pore is eddy free (type-2 in Fig. 10c). In part-III, the streaks of peak  $tr(\tau_p)$  in both top and bottom regions of the pore are close to the walls and their peak values are much smaller than the global maximum of  $tr(\tau_p)$ (Fig.10d). In this case, the pore exhibits an eddy free flow state (type-3 in Fig. 10c). Part-IV also has a single region where maximum value of trace of polymer stress occurs, but it lies on the bottom region of the pore. This stress distribution leads to the pattern where bottom region of the pore has an eddy and the top region of the pore is eddy free (type-4 in Fig. 10c). Fig. 10d also shows that the eddy free flow state (type-3) exists for a shorter time compared to other flow states.

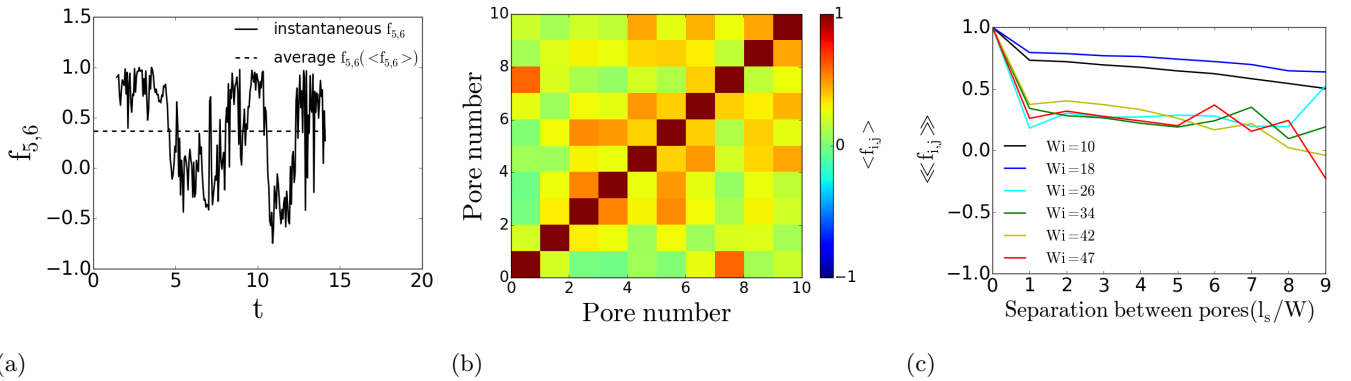


FIG. 11: (a) Instantaneous  $f_{5,6}$  and time-average  $\langle f_{5,6} \rangle$  values of the correlation function between pore 5 and pore 6 at  $Wi = 34$ . (b) The time average value of correlation function for different pairs of the pores at  $Wi = 34$ . (c) The value of  $\langle f_{i,j} \rangle$ , further averaged across the pores of the same separation, as a function of pore separation at different  $Wi$ .

We study the correlation between the area of eddies for different pairs of pores. To quantify the correlation between the area of eddies of two pores, we modify the correlation function (equation 7)  $f_{i,j}$  as:

$$f_{i,j} = 1 - \frac{2|(A_{eddy}/A_{pore})_i - (A_{eddy}/A_{pore})_j|}{\max((A_{eddy}/A_{pore})_i, (A_{eddy}/A_{pore})_j)}. \quad (8)$$

The value of correlation function  $f_{i,j}$  varies from +1 in the case where both the pores have similar eddy pattern to -1 in the case where one pore has an eddy and the other is eddy free. The value of  $f_{i,j}$  varies with time for any given pair of pores, which indicates the transient nature of the correlation between the pores (Fig. 11a). Therefore, the pattern of eddies inside the pores exhibits both positive and negative correlations. We use the time average of  $f_{i,j}$  ( $\langle f_{i,j} \rangle$ ) to study the statistics of the correlations between the eddies of two pores in a long time. Figure 11b depicts the time average value of  $f_{i,j}$  for different pairs of pores at  $Wi = 34$ . There is a relatively stronger positive correlation between the eddies' area of the nearby pores and the correlation weakens as the separation between the pores increases. Conversely, we also notice a relatively weak correlation between pore-8 and pore-9 ( $\langle f_{8,9} \rangle = 0.17$ ) and relatively strong correlation between pore-1 and pore-8 ( $\langle f_{1,8} \rangle = 0.6$ ) at  $Wi = 34$  (Fig. 11b). To further investigate the effect of  $Wi$  and the pores' separation on the correlation, we plot  $\langle\langle f_{i,j} \rangle\rangle$  as the function of pore separation at different  $Wi$ , where  $\langle\langle f_{i,j} \rangle\rangle$  is the value of  $\langle f_{i,j} \rangle$  averaged across the pores of the same separation (Fig. 11c). At  $Wi < Wi_{cr}$ , the correlation between the flow patterns inside the pores is stronger compare to  $Wi > Wi_{cr}$  and  $\langle\langle f_{i,j} \rangle\rangle$  monotonically decreases as the separation between the pores increases. For  $Wi > Wi_{cr}$ , irrespective of separation between the pores, the correlation is weak (i.e.,  $\langle\langle f_{i,j} \rangle\rangle < 0.5$ ) (Fig. 11c).

We have also plotted the probability distribution of the area occupied by eddies inside each individual pore in the channel of 10 closely located pores at different  $Wi$  (Fig. 12a). The value of  $A_{eddy}/A_{pore}$  ranges 0.1-0.25 at  $Wi = 18$ , whereas it varies from 0.0 (eddy free pattern) to 0.5 at  $Wi = 47$ . The eddy does not disappear in either regions of

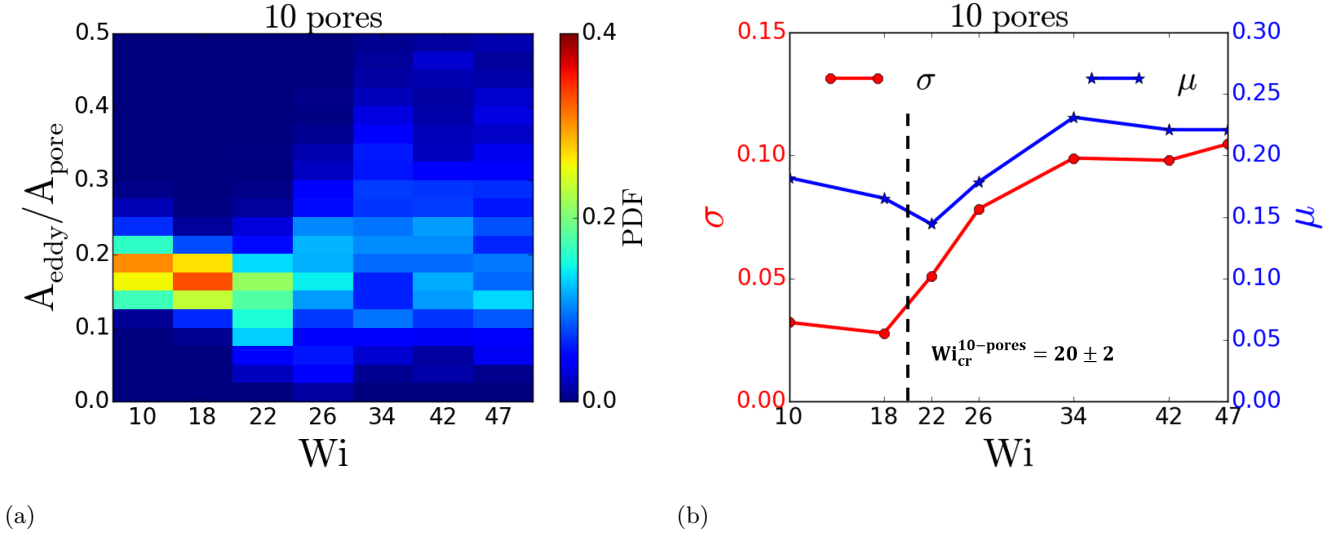


FIG. 12: (a) PDF of the ratio of eddies to pore area ( $A_{\text{eddy}}/A_{\text{pore}}$ ) at different  $Wi$  for a channel of 10 closely located pores.  $A_{\text{eddy}}$  represents total area occupied by eddies in an individual pore and  $A_{\text{pore}}$  is the total area of the pore. Above a threshold  $Wi$ , there appears to be multistability, and the eddy areas take on a broad range of values. (b) Mean ( $\mu$ ) and standard deviation ( $\sigma$ ) of normalized eddies' area.

the pore at  $Wi < Wi_{\text{cr}}$ , while often it disappears at  $Wi > Wi_{\text{cr}}$ . Thus, the area of eddies and flow pattern inside the pores are highly predictable for  $Wi < Wi_{\text{cr}}$ , but not at  $Wi > Wi_{\text{cr}}$ . We have calculated the standard deviation ( $\sigma$ ) and mean ( $\mu$ ) of  $A_{\text{eddy}}/A_{\text{pore}}$  in Fig. 12b to quantify the fluctuation of eddies' area. The standard deviation of eddies' area increases with  $Wi$  for  $Wi > Wi_{\text{cr}}$  and the onset of the increase of  $\sigma$  lies between  $Wi = 18 - 22$ . Therefore, we consider  $Wi_{\text{cr}} = 20 \pm 2$  as the critical  $Wi$  of the multistability. The threshold  $Wi$ , above which multistability appears, for the channel of 10 closely located pores ( $Wi_{\text{cr}} = 20 \pm 2$ ) (Fig. 12b) is smaller than the channel with single or two widely separated throats ( $Wi_{\text{cr}} = 28 \pm 2$ ) (Fig. 3b and 7b). When the pores are closer to each other, the onset of multistability arises at lower  $Wi$ , due to the advection of polymer stress between the pores. Similar observation was reported in experiments [47]. We have also noticed that sometime eddies appear even at the center of the pore with/without eddies on the top or bottom region of the pore at  $Wi > Wi_{\text{cr}}$  ( Fig. 13). This behavior has not been reported in prior experimental studies.

The pressure drop of the flow inside the porous media is an important macroscopic property due to practical application in the field of oil recovery [6] and ground water remediation [7, 8]. To understand the spatial distribution of pressure, we have plotted the contours of dimensionless pressure ( $p$ ) in Fig. 14a for the flow field shown in Fig. 8b (i.e.,  $Wi = 34, \tau \approx 10$ ). We have also plotted the pressure profile along the centerline of the channel (i.e., red solid line in Fig. 14a) (Fig. 14b) and at the center of the pore along the width (i.e., dashed yellow line in Fig. 14a) (Fig. 14c). The pressure inside the channel does not decrease monotonically due to the converging-diverging geometry of the channel (Fig. 14b). For the cross-section at the center of an individual pore, the pressure is maximum at the centerline (i.e.,  $y = 0$ ) of the channel (Fig. 14c). Instantaneous pressure drop across the channel along the centerline ( $\Delta p$  in Fig. 14a) is transient due to instability and the fluctuation intensifies as  $Wi$  increases (Fig. 15a). We calculate the time averaged pressure drop ( $\langle \Delta p \rangle$ ) along with fluctuations across the channel for a fixed volumetric flow rate at different  $Wi$  (Fig. 15b). The instability inside the pores facilitates the flow and lowers the hydrodynamic drag, which leads to a smaller pressure drop across the channel as  $Wi$  increases (Fig. 15b). To further understand the mechanism of hydrodynamic drag reduction with increasing  $Wi$ , we calculate the pressure drop across individual pores along the centerline of the channel (specially, pore-8 and pore-9 as depicted in Fig. 14a) for the flow state shown in Fig. 8b. The pressure drop across an eddy free pore is smaller than the pressure drop across the pore with eddies (Example:  $\Delta p_{\text{pore-9}} = 3.45$  for pore-9 shown in Fig. 8b and  $\Delta p_{\text{pore-8}} = 4.6$  for pore-8 shown in Fig. 8b). Because, the eddy free pore has larger apparent width involve in the net volumetric flow (i.e., fluid circulates inside an eddy and does not contribute in any net volumetric flow) and the pressure drop in the channel is inversely related to its apparent width. The presence of eddy free pores at  $Wi > Wi_{\text{cr}}$  leads to smaller pressure drop across the channel, in contrast with a channel at  $Wi < Wi_{\text{cr}}$  where all the pores have eddies. We have also calculated the pressure drop in single and double throated channels for the length same as the channel of 10 pores. The pressure drop in the single as well as double throated channel is much smaller due to lesser constriction and it also decreases with  $Wi$  due to

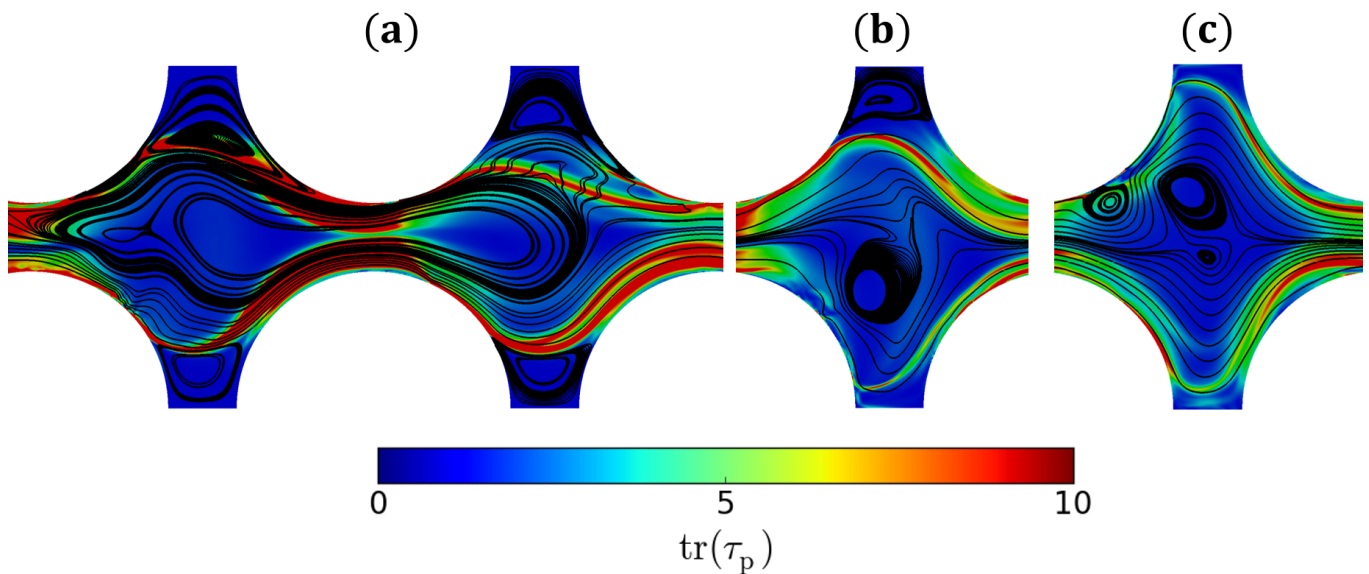


FIG. 13: Eddies at the center of the pore at  $Wi = 34$ . (a) Eddy at the center as well as the top and bottom regions of the pore. Here, the eddy at the center persists in two pores. (b) Eddies at the center and the top region of the pore, while bottom region is eddy free. (c) Eddies only at the center of the pore. Top and bottom regions are eddy free.

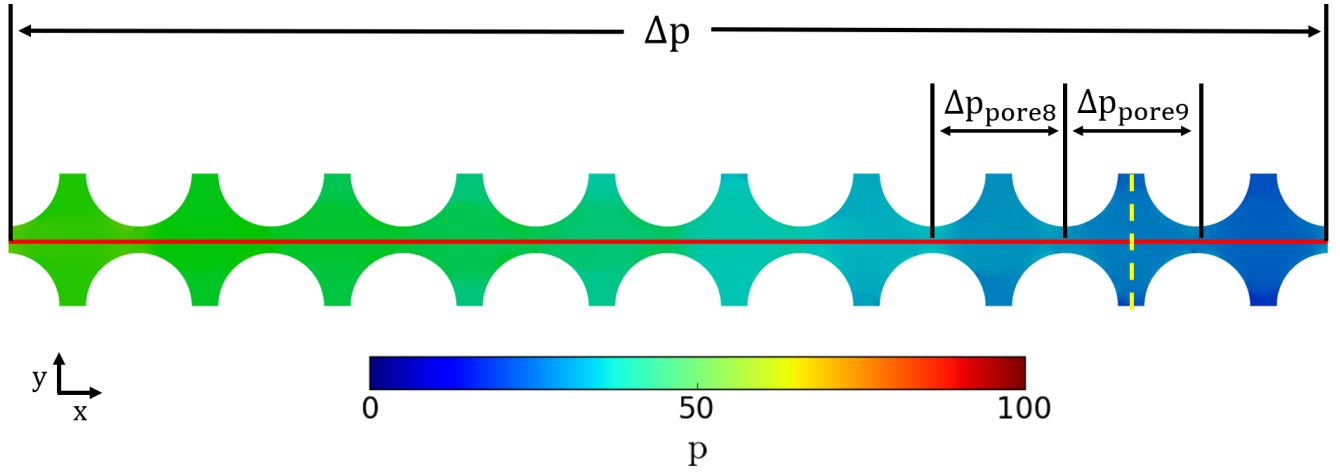
instability (Fig. 15b).

## V. CONCLUSIONS

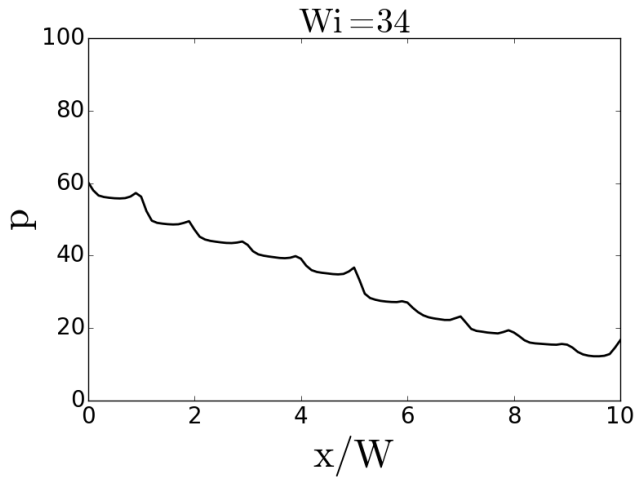
We numerically study the flow of a polymeric fluid in channels consisting of converging and diverging physical constraints. We use channels with a single pore throat, two widely separated pore throats and ten closely separated pores to study an elastic-induced flow instability at different  $Wi$ . The channels with either a single pore throat or two widely separated pore throats have unstable eddies in the upstream of the pore throats whose average length ( $L_{\text{eddy}}$ ) increases with  $Wi$ . In the case of 10 closely placed pores, eddies appear on both top and bottom regions of the pores at  $Wi < Wi_{\text{cr}}$ , whereas the flow exhibits 4 distinct types of patterns inside the pores at  $Wi > Wi_{\text{cr}}$ . The eddies on both the top and bottom regions of the pores regularly collapse and reform at  $Wi > Wi_{\text{cr}}$ . This behavior of eddies leads to flow patterns where eddies appear in either one region, both regions, or neither region of the pore (eddy free). The high polymeric stress region inside the pore induces eddy formation, whereas the high stress region close to the walls leads to eddy collapse. There is a positive correlation between the eddy areas of neighboring pores in the long-time statistics, but this correlation weakens as the separation between the pores increases. The correlation between the pores also weakens as  $Wi$  increases. The eddy free pores also lead to reduced hydrodynamic drag across the channel at  $Wi > Wi_{\text{cr}}$ . Disorder of the porous media is expected to play a large role in altering the instability, and would be an interesting parameter to consider in a future study [59, 82].

## VI. ACKNOWLEDGEMENTS

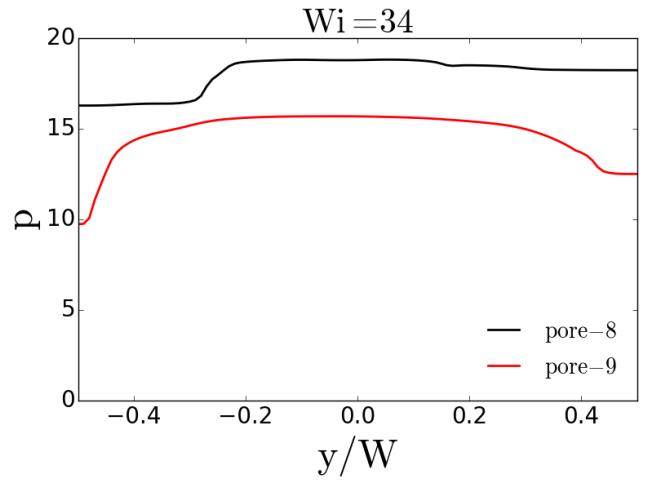
A.M. Ardekani would like to acknowledge the financial support from the National Science Foundation (CBET-1700961 and CBET-1705371). M.K. was also supported in part by the Ross graduate fellowship from Purdue College of Engineering. This work used the Extreme Science and Engineering Discovery Environment (XSEDE) [110], which is supported by the National Science Foundation grant number ACI-1548562 through allocation TG-CTS180066 and TG-CTS190041 to A.M.A. Acknowledgment is made to the Donors of the American Chemical Society Petroleum Research Fund for partial support of this research to S.S.D. and C.A.B through grant PRF 59026-DNI9. This material is also based upon work supported by the National Science Foundation Graduate Research Fellowship Program (to C.A.B.) under Grant No. DGE1656466. Any opinions, findings, and conclusions or recommendations expressed in this material are those of the authors and do not necessarily reflect the views of the National Science Foundation. C.A.B.



(a)



(b)



(c)

FIG. 14: Dimensionless pressure for the flow field shown in Fig. 8b (i.e.,  $Wi = 34$ ,  $t \approx 10$ ): (a) The contours of pressure field inside the channel. (b) Pressure along the centerline of the channel (i.e. red solid line in Fig. 14a). (c) Pressure across the channel at the center of the pore (i.e. dashed yellow line in Fig. 14a).

was also supported in part by the Mary and Randall Hack Graduate Award of the High Meadows Environmental Institute.

## VII. APPENDIX

### A. Start up transient flow

We use pressure drop ( $\Delta p$ ) across the channel along the centerline as a simple metric to characterize the transient start up flow. The flow reaches steady state for  $t > 0.2$  at  $Wi = 0.3$  (almost Newtonian fluid) (Fig. 16a). For fluctuating flows, the meaning of fully developed flow is that fluctuating quantities have a well-defined mean. The instability becomes fully developed for  $t > 1$  as  $\Delta p$  fluctuates around a mean for  $t > 1$  (Fig. 16b).

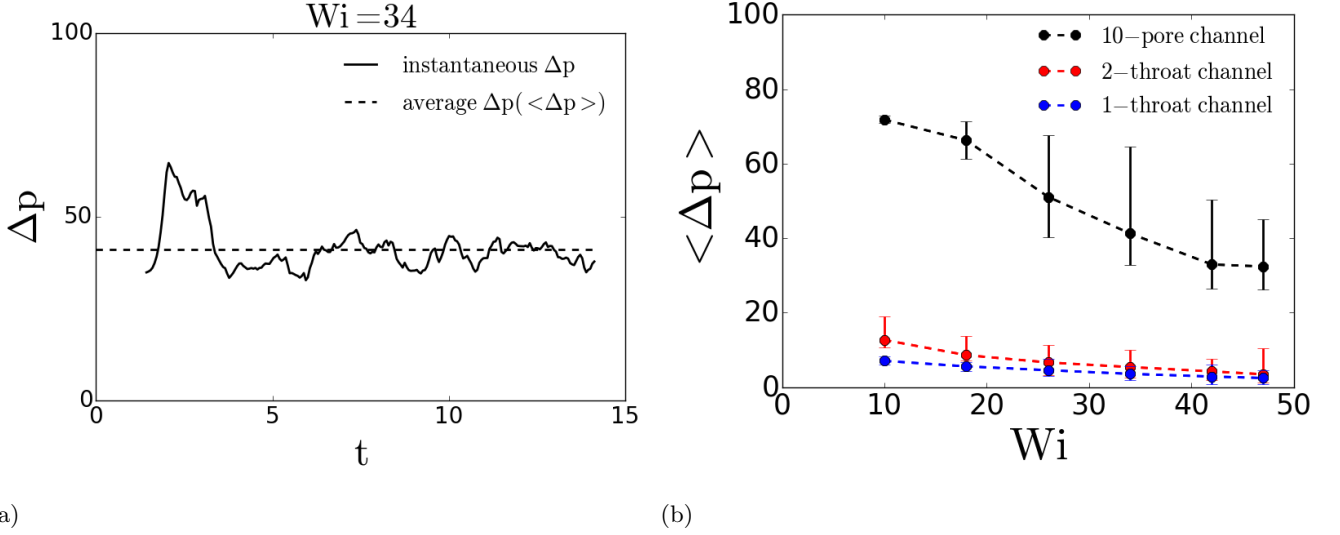


FIG. 15: (a) Instantaneous and time averaged pressure drop across the channel of 10 pores at  $Wi = 34$ . (b) Averaged pressure drop ( $\langle \Delta p \rangle$ ) across the channels at different  $Wi$ .

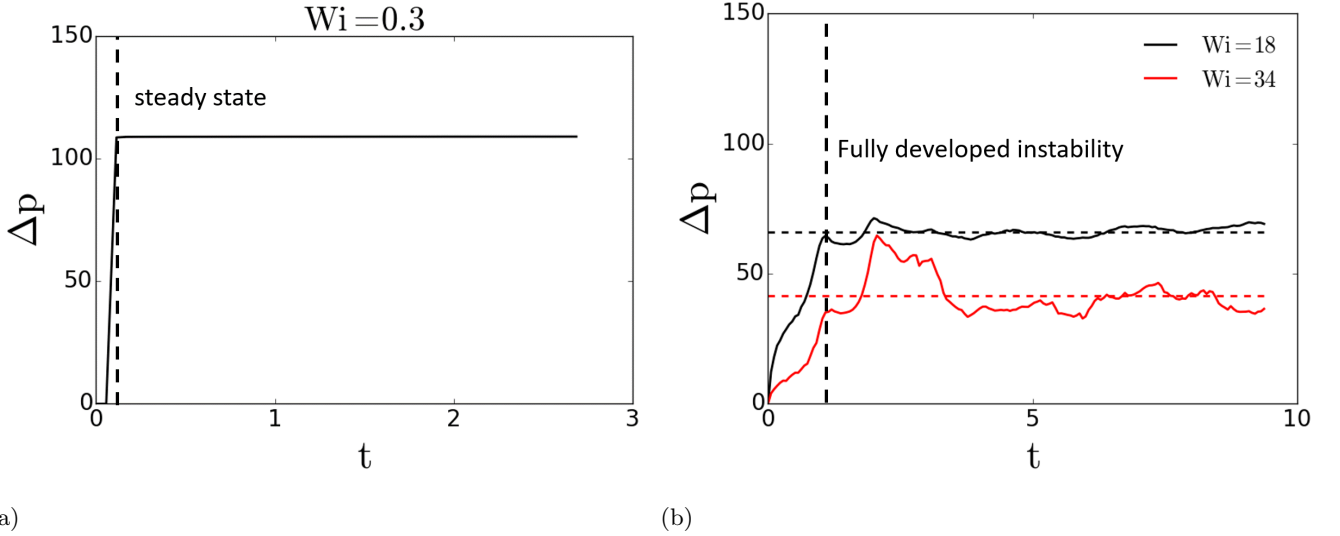


FIG. 16: (a) Dimensionless pressure drop across the channel along the centerline at  $Wi = 0.3$  (almost Newtonian fluid). Flow converges to steady state for  $t > 0.2$ . (b) Dimensionless pressure drop across the channel along the centerline at  $Wi = 18, 34$ . Fully developed instability occurs for  $t > 1$ .

### B. Eddy area at $Wi = 0.3$ (almost Newtonian fluid)

### C. Flow of non-shear thinning fluid (FENE-CR) inside the pores

We have also performed a simulation for non-shear thinning model (FENE-CR) at relaxation time  $\lambda = 0.2s$ , viscosity ratio  $\beta = \eta_s/(\eta_s + \eta_p) = 0.01$ ,  $L^2 = 625$  and volumetric flow rate per unit depth of the channel  $Q = 16.8 \text{ mm}^2/\text{s}$ . These parameters lead to  $Wi = 16.4$  for FENE-CR model [111]. This model also exhibits multistability similar to FENE-P model (Fig. 18). Fig. 18a shows eddy free flow state. Fig. 18b has eddy only on the bottom region of the pore and top region is eddy free. Fig. 18c has eddies on both top and bottom region of the pore, whereas Fig. 18d represents the flow state where eddy appears only on the top region of the pore and bottom region is eddy free. Non-shear thinning fluid (FENE-CR) also exhibits the flow state wherein the eddy appears at the center of the pore (Fig. 18e).



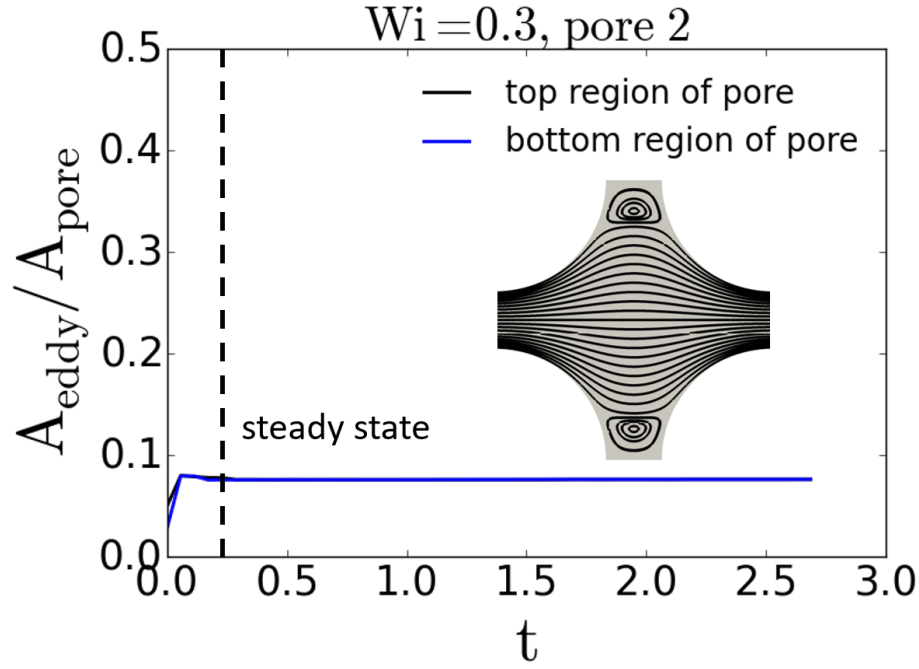


FIG. 17: The area of eddies on the top and bottom of “pore-2” at  $Wi = 0.3$ .

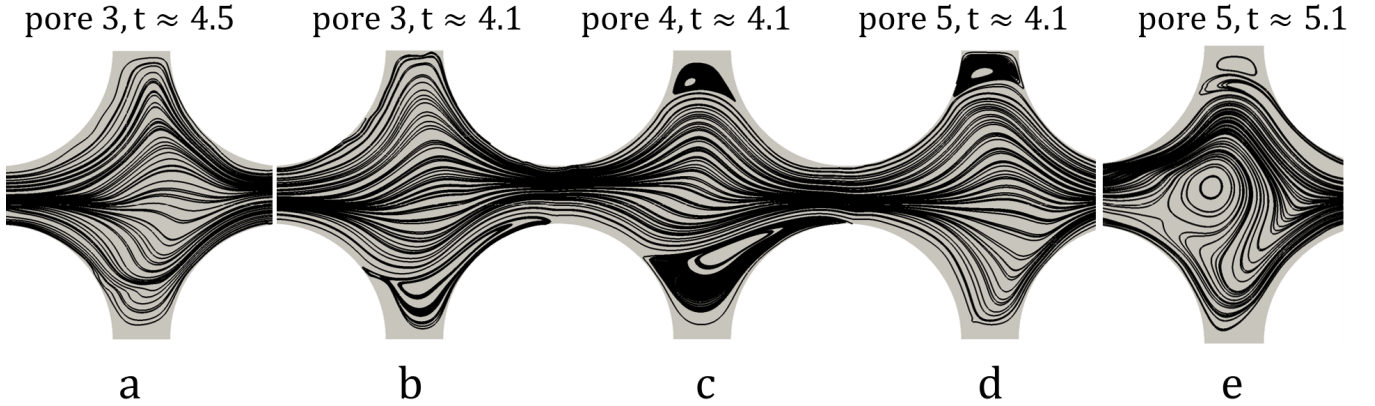


FIG. 18: Instantaneous streamlines in a channel of 10 closely interconnected pores at  $Wi = 16.4$  for FENE-CR constitutive model.

- 
- [1] C. A. Browne, A. Shih, and S. S. Datta, Pore-scale flow characterization of polymer solutions in microfluidic porous media, *Small*, 1903944 (2019).
  - [2] C. M. Schroeder, Single polymer dynamics for molecular rheology, *Journal of Rheology* **62**, 371 (2018).
  - [3] S. J. Haward, Microfluidic extensional rheometry using stagnation point flow, *Biomicrofluidics* **10**, 043401 (2016).
  - [4] J. R. A. Pearson, Instability in non-newtonian flow, *Annual Review of Fluid Mechanics* **8**, 163 (1976).
  - [5] R. G. Larson, Flow-induced mixing, demixing, and phase transitions in polymeric fluids, *Rheologica Acta* **31**, 497 (1992).
  - [6] K. S. Sorbie, *Polymer-improved oil recovery* (Springer Science & Business Media, 2013).
  - [7] D. Roote, Technology status report: in situ flushing, Ground Water Remediation Technology Analysis Center (available at <http://www.gwrtac.org>) (1998).
  - [8] M. M. Smith, J. A. Silva, J. Munakata-Marr, and J. E. McCray, Compatibility of polymers and chemical oxidants for enhanced groundwater remediation, *Environmental science & technology* **42**, 9296 (2008).

- [9] B. Sandiford *et al.*, Laboratory and field studies of water floods using polymer solutions to increase oil recoveries, *Journal of Petroleum Technology* **16**, 917 (1964).
- [10] F. Durst, R. Haas, and B. Kaczmar, Flows of dilute hydrolyzed polyacrylamide solutions in porous media under various solvent conditions, *Journal of Applied Polymer Science* **26**, 3125 (1981).
- [11] M. J. Pitts, T. A. Campbell, H. Surkalo, K. Wyatt, *et al.*, Polymer flood of the rapdan pool, saskatchewan, canada, *SPE Reservoir Engineering* **10**, 183 (1995).
- [12] D. Wang, G. Wang, H. Xia, *et al.*, Large scale high visco-elastic fluid flooding in the field achieves high recoveries, in *SPE Enhanced Oil Recovery Conference* (Society of Petroleum Engineers, 2011).
- [13] B. Wei, L. Romero-Zerón, and D. Rodrigue, Oil displacement mechanisms of viscoelastic polymers in enhanced oil recovery (eor): a review, *Journal of Petroleum Exploration and Production Technology* **4**, 113 (2014).
- [14] E. Vermolen, M. Van Haasterecht, S. Masalmeh, *et al.*, A systematic study of the polymer visco-elastic effect on residual oil saturation by core flooding, in *SPE EOR Conference at Oil and Gas West Asia* (Society of Petroleum Engineers, 2014).
- [15] L. J. Fauci and R. Dillon, Biofluidmechanics of Reproduction, *Annual Review of Fluid Mechanics* **38**, 371 (2006).
- [16] D. J. Smith, E. A. Gaffney, and J. R. Blake, Modelling mucociliary clearance, *Respiratory Physiology and Neurobiology* **163**, 178 (2008).
- [17] M. J. Blunt, *Multiphase flow in permeable media: A pore-scale perspective* (Cambridge University Press, 2017).
- [18] S. S. Datta, H. Chiang, T. Ramakrishnan, and D. A. Weitz, Spatial fluctuations of fluid velocities in flow through a three-dimensional porous medium, *Physical review letters* **111**, 064501 (2013).
- [19] P. K. Kang, P. de Anna, J. P. Nunes, B. Bijeljic, M. J. Blunt, and R. Juanes, Pore-scale intermittent velocity structure underpinning anomalous transport through 3-d porous media, *Geophysical Research Letters* **41**, 6184 (2014).
- [20] T. Pak, I. B. Butler, S. Geiger, M. I. van Dijke, and K. S. Sorbie, Droplet fragmentation: 3d imaging of a previously unidentified pore-scale process during multiphase flow in porous media, *Proceedings of the National Academy of Sciences* **112**, 1947 (2015).
- [21] F. Zami-Pierre, R. De Loubens, M. Quintard, and Y. Davit, Transition in the flow of power-law fluids through isotropic porous media, *Physical review letters* **117**, 074502 (2016).
- [22] A. M. Howe, A. Clarke, and D. Giernalczyk, Flow of concentrated viscoelastic polymer solutions in porous media: effect of mw and concentration on elastic turbulence onset in various geometries, *Soft Matter* **11**, 6419 (2015).
- [23] J. Mitchell, K. Lyons, A. M. Howe, and A. Clarke, Viscoelastic polymer flows and elastic turbulence in three-dimensional porous structures, *Soft Matter* **12**, 460 (2016).
- [24] A. Clarke, A. M. Howe, J. Mitchell, J. Staniland, L. A. Hawkes, *et al.*, How viscoelastic-polymer flooding enhances displacement efficiency, *SPE Journal* **21**, 675 (2016).
- [25] S. S. Datta, J.-B. Dupin, and D. A. Weitz, Fluid breakup during simultaneous two-phase flow through a three-dimensional porous medium, *Physics of Fluids* **26**, 062004 (2014).
- [26] S. S. Datta, T. Ramakrishnan, and D. A. Weitz, Mobilization of a trapped non-wetting fluid from a three-dimensional porous medium, *Physics of Fluids* **26**, 022002 (2014).
- [27] A. Bourgeat, O. Gipouloux, and E. Marusic-Paloka, Filtration law for polymer flow through porous media, *Multiscale Modeling & Simulation* **1**, 432 (2003).
- [28] B. G. Compton and J. A. Lewis, 3d-printing of lightweight cellular composites, *Advanced materials* **26**, 5930 (2014).
- [29] X. Wang, M. Jiang, Z. Zhou, J. Gou, and D. Hui, 3d printing of polymer matrix composites: A review and prospective, *Composites Part B: Engineering* **110**, 442 (2017).
- [30] G. H. McKinley, P. Pakdel, and A. Öztekin, Rheological and geometric scaling of purely elastic flow instabilities, *Journal of Non-Newtonian Fluid Mechanics* **67**, 19 (1996).
- [31] P. Pakdel and G. H. McKinley, Elastic instability and curved streamlines, *Physical Review Letters* **77**, 2459 (1996).
- [32] R. G. Larson, E. S. Shaqfeh, and S. J. Muller, A purely elastic instability in taylor-couette flow, *Journal of Fluid Mechanics* **218**, 573 (1990).
- [33] S. J. Haward and J. A. Odell, Viscosity enhancement in non-newtonian flow of dilute polymer solutions through crystallographic porous media, *Rheologica acta* **42**, 516 (2003).
- [34] J. A. Odell and S. J. Haward, Viscosity enhancement in non-newtonian flow of dilute aqueous polymer solutions through crystallographic and random porous media, *Rheologica acta* **45**, 853 (2006).
- [35] C. Huh, G. A. Pope, *et al.*, Residual oil saturation from polymer floods: laboratory measurements and theoretical interpretation, in *SPE Symposium on Improved Oil Recovery* (Society of Petroleum Engineers, 2008).
- [36] A. Zaitoun, N. Kohler, *et al.*, Two-phase flow through porous media: effect of an adsorbed polymer layer, in *SPE Annual Technical Conference and Exhibition* (Society of Petroleum Engineers, 1988).
- [37] A. Zaitoun, H. Bertin, D. Lasseux, *et al.*, Two-phase flow property modifications by polymer adsorption, in *SPE/DOE improved oil recovery symposium* (Society of Petroleum Engineers, 1998).
- [38] G. Chauveteau and M. Moan, The onset of dilatant behaviour in non-inertial flow of dilute polymer solutions through channels with varying cross-sections, *Journal de Physique Lettres* **42**, 201 (1981).
- [39] G. Chauveteau, M. Moan, and A. Magueur, Thickening behaviour of dilute polymer solutions in non-inertial elongational flows, *Journal of non-newtonian fluid mechanics* **16**, 315 (1984).
- [40] R. Haas and F. Durst, Viscoelastic flow of dilute polymer solutions in regularly packed beds, *Rheologica Acta* **21**, 566 (1982).

- [41] N. E. Dyakonova, J. A. Odell, Y. V. Brestkin, A. V. Lyulin, and A. E. Saez, Macromolecular strain in periodic models of porous media flows, *Journal of Non-Newtonian Fluid Mechanics* **67**, 285 (1996).
- [42] M. G. Saphiannikova, A. A. Darinskii, and N. E. Dyakonova, Computer simulation of dilute polymer solutions in transient elongational flows, *Macromolecular Theory and Simulations* **9**, 270 (2000).
- [43] X. Shi, S. Kenney, G. Chapagain, and G. F. Christopher, Mechanisms of onset for moderate mach number instabilities of viscoelastic flows around confined cylinders, *Rheologica Acta* **54**, 805 (2015).
- [44] X. Shi and G. F. Christopher, Growth of viscoelastic instabilities around linear cylinder arrays, *Physics of Fluids* **28**, 124102 (2016).
- [45] A. Varshney and V. Steinberg, Elastic wake instabilities in a creeping flow between two obstacles, *Physical Review Fluids* **2**, 051301 (2017).
- [46] B. Qin, P. F. Salipante, S. D. Hudson, and P. E. Arratia, Upstream vortex and elastic wave in the viscoelastic flow around a confined cylinder, *Journal of Fluid Mechanics* **864** (2019).
- [47] C. A. Browne, A. Shih, and S. S. Datta, Bistability in the unstable flow of polymer solutions through pore constriction arrays, *Journal of Fluid Mechanics* **890**, 10.1017/jfm.2020.122 (2020).
- [48] E. M. Ekanem, S. Berg, S. De, A. Fadili, T. Bultreys, M. Rücker, J. Southwick, J. Crawshaw, and P. F. Luckham, Signature of elastic turbulence of viscoelastic fluid flow in a single pore throat, *Physical Review E* **101**, 42605 (2020).
- [49] G. Batchelor, The stress generated in a non-dilute suspension of elongated particles by pure straining motion, *Journal of Fluid Mechanics* **46**, 813 (1971).
- [50] D. V. Boger, Viscoelastic Flows Through Contractions, *Annual Review of Fluid Mechanics* **19**, 157 (1987).
- [51] A. Mongruel and M. Cloitre, Extensional flow of semidilute suspensions of rod-like particles through an orifice, *Physics of Fluids* **7**, 2546 (1995).
- [52] A. Mongruel and M. Cloitre, Axisymmetric orifice flow for measuring the elongational viscosity of semi-rigid polymer solutions, *Journal of Non-Newtonian Fluid Mechanics* **110**, 27 (2003).
- [53] L. Rodd, J. Cooper-White, D. Boger, and G. McKinley, Role of the elasticity number in the entry flow of dilute polymer solutions in micro-fabricated contraction geometries, *Journal of Non-Newtonian Fluid Mechanics* **143**, 170 (2007).
- [54] K. Weissenberg, A continuum theory of rheological phenomena (1947).
- [55] A. Groisman and V. Steinberg, Elastic turbulence in a polymer solution flow, *Nature* **405**, 53 (2000).
- [56] A. Groisman and V. Steinberg, Efficient mixing at low reynolds numbers using polymer additives, *Nature* **410**, 905 (2001).
- [57] A. Groisman and V. Steinberg, Elastic turbulence in curvilinear flows of polymer solutions, *New Journal of Physics* **6**, 29 (2004).
- [58] R. Poole, The Deborah and Weissenberg numbers, *British Soc. Rheol. Rheol. Bull* **53**, 32 (2012).
- [59] D. M. Walkama, N. Waisbord, and J. S. Guasto, Disorder suppresses chaos in viscoelastic flows, *Physical Review Letters* **124**, 164501 (2020).
- [60] B. Qin, P. F. Salipante, S. D. Hudson, and P. E. Arratia, Flow resistance and structures in viscoelastic channel flows at low re, *Physical review letters* **123**, 194501 (2019).
- [61] B. Qin and P. E. Arratia, Characterizing elastic turbulence in channel flows at low reynolds number, *Physical Review Fluids* **2**, 083302 (2017).
- [62] L. Pan, A. Morozov, C. Wagner, and P. Arratia, Nonlinear elastic instability in channel flows at low reynolds numbers, *Physical review letters* **110**, 174502 (2013).
- [63] D. Kawale, E. Marques, P. L. Zitha, M. T. Kreutzer, W. R. Rossen, and P. E. Boukany, Elastic instabilities during the flow of hydrolyzed polyacrylamide solution in porous media: Effect of pore-shape and salt, *Soft matter* **13**, 765 (2017).
- [64] D. Kawale, G. Bouwman, S. Sachdev, P. L. Zitha, M. T. Kreutzer, W. R. Rossen, and P. E. Boukany, Polymer conformation during flow in porous media, *Soft matter* **13**, 8745 (2017).
- [65] Y. Lam, H. Gan, N.-T. Nguyen, and H. Lie, Micromixer based on viscoelastic flow instability at low reynolds number, *Biomicrofluidics* **3**, 014106 (2009).
- [66] N. P. Teclerian, V. A. Beck, E. S. Shaqfeh, and S. J. Muller, Dynamics of dna polymers in post arrays: Comparison of single molecule experiments and simulations, *Macromolecules* **40**, 3848 (2007).
- [67] J. Zilz, R. Poole, M. Alves, D. Bartolo, B. Levaché, and A. Lindner, Geometric scaling of a purely elastic flow instability in serpentine channels, *Journal of Fluid Mechanics* **712**, 203 (2012).
- [68] F. J. Galindo-Rosales, L. Campo-Deaño, F. Pinho, E. Van Bokhorst, P. Hamersma, M. S. Oliveira, and M. Alves, Microfluidic systems for the analysis of viscoelastic fluid flow phenomena in porous media, *Microfluidics and nanofluidics* **12**, 485 (2012).
- [69] V. Ribeiro, P. Coelho, F. Pinho, and M. Alves, Viscoelastic fluid flow past a confined cylinder: Three-dimensional effects and stability, *Chemical engineering science* **111**, 364 (2014).
- [70] A. Lanzaro and X.-F. Yuan, Effects of contraction ratio on non-linear dynamics of semi-dilute, highly polydisperse paam solutions in microfluidics, *Journal of Non-Newtonian Fluid Mechanics* **166**, 1064 (2011).
- [71] A. Lanzaro and X.-F. Yuan, A quantitative analysis of spatial extensional rate distribution in nonlinear viscoelastic flows, *Journal of Non-Newtonian Fluid Mechanics* **207**, 32 (2014).
- [72] A. Lanzaro, Z. Li, and X.-F. Yuan, Quantitative characterization of high molecular weight polymer solutions in microfluidic hyperbolic contraction flow, *Microfluidics and Nanofluidics* **18**, 819 (2015).
- [73] A. Lanzaro, D. Corbett, and X.-F. Yuan, Non-linear dynamics of semi-dilute paam solutions in a microfluidic 3d cross-slot flow geometry, *Journal of Non-Newtonian Fluid Mechanics* **242**, 57 (2017).
- [74] S. J. Haward, C. C. Hopkins, and A. Q. Shen, Asymmetric flow of polymer solutions around microfluidic cylinders: Interaction between shear-thinning and viscoelasticity, *Journal of Non-Newtonian Fluid Mechanics* **278**, 104250 (2020).

- [75] S. J. Haward, N. Kitajima, K. Toda-Peters, T. Takahashi, and A. Q. Shen, Flow of wormlike micellar solutions around microfluidic cylinders with high aspect ratio and low blockage ratio, *Soft Matter* **15**, 1927 (2019).
- [76] S. Aramideh, P. P. Vlachos, and A. M. Ardekani, Nanoparticle dispersion in porous media in viscoelastic polymer solutions, *Journal of Non-Newtonian Fluid Mechanics* **268**, 75 (2019).
- [77] S. De, P. Krishnan, J. van der Schaaf, J. Kuipers, E. Peters, and J. Padding, Viscoelastic effects on residual oil distribution in flows through pillared microchannels, *Journal of colloid and interface science* **510**, 262 (2018).
- [78] S. De, S. Koesen, R. Maitri, M. Golombok, J. Padding, and J. van Santvoort, Flow of viscoelastic surfactants through porous media, *AIChE Journal* **64**, 773 (2018).
- [79] S. De, J. Kuipers, E. Peters, and J. Padding, Viscoelastic flow simulations in random porous media, *Journal of Non-Newtonian Fluid Mechanics* **248**, 50 (2017).
- [80] S. De, J. Kuipers, E. Peters, and J. Padding, Viscoelastic flow simulations in model porous media, *Physical Review Fluids* **2**, 053303 (2017).
- [81] S. De, J. van der Schaaf, N. Deen, J. Kuipers, E. Peters, and J. Padding, Elastic instabilities in flows through pillared micro channels, arXiv preprint arXiv:1607.03672 (2016).
- [82] F. Babayekhorasani, D. E. Dunstan, R. Krishnamoorti, and J. C. Conrad, Nanoparticle dispersion in disordered porous media with and without polymer additives, *Soft Matter* **12**, 5676 (2016).
- [83] S. Kenney, K. Poper, G. Chapagain, and G. F. Christopher, Large Deborah number flows around confined microfluidic cylinders, *Rheologica Acta* **52**, 485 (2013).
- [84] S. Varchanis, C. C. Hopkins, A. Q. Shen, J. Tsamopoulos, and S. J. Haward, Asymmetric flows of complex fluids past confined cylinders: A comprehensive numerical study with experimental validation, *Physics of Fluids* **32**, 053103 (2020).
- [85] M. Avgousti and A. N. Beris, Non-axisymmetric modes in viscoelastic taylor-couette flow, *Journal of non-newtonian fluid mechanics* **50**, 225 (1993).
- [86] R. Sureshkumar, A. N. Beris, and M. Avgousti, Non-axisymmetric subcritical bifurcations in viscoelastic taylor-couette flow, *Proceedings of the Royal Society of London. Series A: Mathematical and Physical Sciences* **447**, 135 (1994).
- [87] K.-W. Hsiao, C. Sasmal, J. Ravi Prakash, and C. M. Schroeder, Direct observation of dna dynamics in semidilute solutions in extensional flow, *Journal of Rheology* **61**, 151 (2017).
- [88] N. François, D. Lasne, Y. Amarouchene, B. Lounis, and H. Kellay, Drag enhancement with polymers, *Physical review letters* **100**, 018302 (2008).
- [89] Y. Liu, Y. Jun, and V. Steinberg, Longest relaxation times of double-stranded and single-stranded dna, *Macromolecules* **40**, 2172 (2007).
- [90] C. M. Schroeder, H. P. Babcock, E. S. Shaqfeh, and S. Chu, Observation of polymer conformation hysteresis in extensional flow, *Science* **301**, 1515 (2003).
- [91] H. P. Babcock, R. E. Teixeira, J. S. Hur, E. S. Shaqfeh, and S. Chu, Visualization of molecular fluctuations near the critical point of the coil-stretch transition in polymer elongation, *Macromolecules* **36**, 4544 (2003).
- [92] J. S. Hur, E. S. Shaqfeh, H. P. Babcock, D. E. Smith, and S. Chu, Dynamics of dilute and semidilute dna solutions in the start-up of shear flow, *Journal of Rheology* **45**, 421 (2001).
- [93] D. E. Smith and S. Chu, Response of flexible polymers to a sudden elongational flow, *Science* **281**, 1335 (1998).
- [94] T. T. Perkins, D. E. Smith, and S. Chu, Single polymer dynamics in an elongational flow, *Science* **276**, 2016 (1997).
- [95] P. J. Oliveira, An exact solution for tube and slit flow of a FENE-P fluid, *Acta Mechanica* **158**, 157 (2002).
- [96] B. Purnode and M. J. Crochet, Polymer solution characterization with the FENE-P model, *Journal of Non-Newtonian Fluid Mechanics* **77**, 1 (1998).
- [97] R. B. Bird, P. J. Dotson, and N. L. Johnson, Polymer solution rheology based on a finitely extensible bead-spring chain model, *Journal of Non-Newtonian Fluid Mechanics* **7**, 213 (1980).
- [98] M. D. Chilcott and J. M. Rallison, Creeping flow of dilute polymer solutions past cylinders and spheres, *Journal of Non-Newtonian Fluid Mechanics* **29**, 381 (1988).
- [99] H. Jasak, A. Jemcov, and Z. Tukovic, Openfoam: A c++ library for complex physics simulations, *International Workshop on Coupled Methods in Numerical Dynamics*, 1 (2007), cited By :275.
- [100] F. Pimenta and M. A. Alves, Stabilization of an open-source finite-volume solver for viscoelastic fluid flows, *Journal of Non-Newtonian Fluid Mechanics* **239**, 85 (2017).
- [101] J. L. Favero, A. R. Secchi, N. S. Cardozo, and H. Jasak, Viscoelastic flow analysis using the software OpenFOAM and differential constitutive equations, *Journal of Non-Newtonian Fluid Mechanics* **165**, 1625 (2010).
- [102] L. E. Rodd, T. P. Scott, D. V. Boger, J. J. Cooper-White, and G. H. McKinley, The inertio-elastic planar entry flow of low-viscosity elastic fluids in micro-fabricated geometries, *Journal of Non-Newtonian Fluid Mechanics* **129**, 1 (2005).
- [103] B. Khomami and L. D. Moreno, Stability of viscoelastic flow around periodic arrays of cylinders, *Rheologica acta* **36**, 367 (1997).
- [104] K. Arora, R. Sureshkumar, and B. Khomami, Experimental investigation of purely elastic instabilities in periodic flows, *Journal of non-newtonian fluid mechanics* **108**, 209 (2002).
- [105] S. J. Haward, K. Toda-Peters, and A. Q. Shen, Steady viscoelastic flow around high-aspect-ratio, low-blockage-ratio microfluidic cylinders, *Journal of Non-Newtonian Fluid Mechanics* **254**, 23 (2018).
- [106] S. J. Haward, G. H. Mckinley, and A. Q. Shen, Elastic instabilities in planar elongational flow of monodisperse polymer solutions, *Scientific Reports* **6**, 1 (2016).
- [107] R. J. Poole, M. A. Alves, and P. J. Oliveira, Purely elastic flow asymmetries, *Physical Review Letters* **99**, 1 (2007).
- [108] G. N. Rocha, R. J. Poole, M. A. Alves, and P. J. Oliveira, On extensibility effects in the cross-slot flow bifurcation, *Journal of Non-Newtonian Fluid Mechanics* **156**, 58 (2009).

- [109] S. J. Haward and G. H. McKinley, Instabilities in stagnation point flows of polymer solutions, *Physics of Fluids* **25**, 10.1063/1.4818151 (2013).
- [110] J. Towns, T. Cockerill, M. Dahan, I. Foster, K. Gaither, A. Grimshaw, V. Hazlewood, S. Lathrop, D. Lifka, G. Peterson, R. Roskies, J. Scott, and N. Wilkins-Diehr, Xsede: accelerating scientific discovery, *Comput. Sci. Eng.* **16**, 62 (2014).
- [111] P. J. Oliveira, Asymmetric flows of viscoelastic fluids in symmetric planar expansion geometries, *Journal of Non-Newtonian Fluid Mechanics* **114**, 33 (2003).